(NASA-CR-4242) AN ALGEBRAIC HOMOTOPY METHOD FOR GENERATING QUASI-THREE-DIMENSIONAL GRIDS FOR HIGH-SPEED CONFIGURATIONS (High Technology Corp.) 80 p

N89-24581

CSCL 20D

Unclas

H1/34 0218044

NASA Contractor Report 4242

An Algebraic Homotopy Method for Generating Quasi-Three-Dimensional Grids for High-Speed Configurations

Anutosh Moitra
High Technology Corporation
Hampton, Virginia

Prepared for
Langley Research Center
under Contract NAS1-18240

National Aeronautics and
Space Administration
Office of Management
Scientific and Technical
Information Division

1989

TABLE OF CONTENTS

	List of Symbols	iv
	List of Figures	v
I.	Introduction	1
II.	Theory and Mathematical Development	4
	Surface Equations	4
	Grid Generation	7
III.	Orthogonality	13
	Introduction	13
	Present Method	16
	Nearly Horizontal Segments	19
	Nearly Vertical Segments	20
IV.	Description of the Algorithm	23
	Body Surface Definition	23
	Grid Generation	24
V.	Examples of Generated Body Segments and Grid Systems	25
	Body Geometries	25
	Computed Grid Examples	28
VI.	Application to Solution of the Euler Equations	33
VII.	Concluding Remarks	34
VIII.	References	35
IX.	Figures	38

PRECEDING PAGE BLANK NOT FILMED

PAGE ii INTENTIONALLY BLANK

List of Symbols

Symbols

C	Analytical blending function.
E	Variable analogous to homotopy parameter.
f,g,n	homotopic mappings.
F,G	Prescribed end shape cross-sections.
I	Index for cross-sectional stations.
$\hat{i}, \hat{j}, \hat{k}$	Unit Cartesian vectors.
M	Mach number.
P	Exponent used to achieve orthogonality.
q	Exponent used to remove intersection of trajectories.
R	Polar representation of end shapes.
t	General parameter, used in defining body surface.
x,y,z	Cartesian coordinates.
α	Angle of attack (degrees).
λ	Size of scaling function in body surface definition.
ϕ	Angular parameter in body surface definition.
η	Homotopy parameter.
τ	circumferential parameter in body surface definition.

Subscripts

a,b	defines domain of t. $t_a \leq t \leq t_b$.
B1,B2	Initial and terminal cross-sections.
f	Base station.
i	Inner boundary.
n	nose station.
o	Outer boundary.

Logic Operators

$\Rightarrow$	Implies
$\wedge$	And
$\vee$	Or
$'$	Not

List of Figures

Figure 1	Schematic representation of body definition.
Figure 2	Schematic diagram of quasi-three-dimensional grid systems
Figure 3	Unstable property: Curve passing through given point.
Figure 4	Unstable property: Nontransversal intersection.
Figure 5	Homotopic perturbation to achieve near-orthogonality.
Figure 5.a	Family of curves before perturbation.
Figure 5.b	Family of curves after perturbation.
Figure 6	Intersection of orthogonal trajectories.
Figure 6.a	Map with intersecting trajectories.
Figure 6.b	Region of intersection.
Figure 6.c	Corresponding intersecting maps.
Figure 7	Modification of coordinates to achieve orthogonality at horizontal and vertical boundaries.
Figure 7.a	Modification of the x-coordinate for horizontal boundaries.
Figure 7.b	Modification of the y-coordinate for vertical boundaries.
Figure 8	Vectors used in orthogonalization process.
Figure 9	Body geometry defined as transition surface.
Figure 10	Normalized end shapes.
Figure 10.a	Normalized nose section at $X = X_N$.
Figure 10.b	Normalized terminal section at $X = X_F$.
Figure 11	Normalized shape of grid outer boundary.
Figure 12	Three-view representation of body with elliptic cross-section.
Figure 13	Three-view representation of spiked forebody.
Figure 14	Three-view representation of blended wing-body geometry: Body 3.
Figure 15	Three-view representation of blended wing-body geometry with complex planforms: Body 4.
Figure 16	Sectional grid for elliptic body.
Figure 17	Sectional grids for Body 3.
Figure 17.a	Station at midlength of body.
Figure 17.b	Station near base.
Figure 18	Sectional grids for Body 4.
Figure 18.a	Station at midlength of body.
Figure 18.b	Station near base.
Figure 19	Sectional grid for semi-elliptic cylinder.
Figure 20	Grid in chord-wise plane of supersonic wing.
Figure 21	Grids for fighter aircraft configuration.
Figure 21.a	Grid in section containing vertical stabilizer.
Figure 21.b	Cut-away view of three-dimensional grid.
Figure 21.c	Fighter aircraft with two planar grids.
Figure 21.d	Planar grid at canopy.
Figure 21.e	Planar grid at tail.
Figure 22	Grid line concentration near surface of elliptic body.
Figure 22.a	Grid line concentration using m = 1.8.
Figure 22.b	Grid line concentration using m = 2.2.
Figure 23	Grid line concentration near surface of blended wing-body geometry.

Figure 23.a	Grid line concentration at midlength, m = 2.0.
Figure 23.b	Grid line concentration near base, m = 2.0.
Figure 24	Grid line concentration for supersonic wing, m = 1.8.
Figure 25	Grid lines clustered at tip of elliptic body.
Figure 26	Grid lines clustered at wing tips of blended wing-body geometry.
Figure 27	Grid line clustering at plane of symmetry of blended wing-body geometry.
Figure 28	Grid line clustering at arbitrary location on blended wing-body geometry.
Figure 29	Partially orthogonalized grid for elliptic body.
Figure 30	Orthogonality near surface of elliptic body.
Figure 31	Orthogonal grid for blended wing-body geometry.
Figure 32	Orthogonality near surface of blended wing-body geometry.
Figure 33	Orthogonalized grid for discretely input wing-body configuration.
Figure 34	Orthogonal grid at wing-tip of discrete wing-body configuration.
Figure 35	Orthogonal C-type grid for supersonic wing.
Figure 36	Orthogonality near leading edge of supersonic wing.
Figure 37	Intersection of orthogonal trajectories in corner regions.
Figure 38	Intersection of trajectories in concave regions and grid distortion.
Figure 39	Smooth grid with intersections removed.
Figure 40	Intersecting normal trajectories for section containing vertical stablizer.
Figure 41	Smooth grid for section with vertical stabilizer with intersections and distortions removed.
Figure 42	Polar-like grid for nozzle with grid clustering.
Figure 43	Grids in exhaust area behind base of blended wing-body configuration.
Figure 44	Continuity between inner and outer grids in exhaust area.
Figure 45	Stacked grids in exhaust region.
Figure 46	Sectional grid for duct with circular cross-section.
Figure 47	Duct geometry with varying cross-sectional shapes.
Figure 48	Duct configuration with sectional grids.
Figure 49	Computed pressure contours for elliptic body M = 1.6, $\alpha = 6^{o}$.
Figure 50	Computed surface pressure on elliptic body. $0^{o} \leq \theta \leq 180^{o}$, M = 2.5, $\alpha = 5^{o}$.
Figure 51	Computed pressure contours for blended wing-body. M = 3.0, $\alpha = 3^{o}$.
Figure 52	Computed pressure contours in planform plane of blended wing-body configuration. M = 3.0, $\alpha = 3^{o}$.
Figure 53	Computed pressure contours for fighter aircraft. M = 1.8, $\alpha = 5^{o}$.

SUMMARY

A fast and versatile procedure for algebraically generating boundary conforming computational grids for use with finite-volume Euler flow solvers is presented. A semi-analytic homotopic procedure is used to generate the grids. Grids generated in two-dimensional planes are stacked to produce quasi-three-dimensional grid systems. The body surface and outer boundary are described in terms of surface parameters. An interpolation scheme is used to blend between the body surface and the outer boundary in order to determine the field points. The method, albeit developed for analytically generated body geometries is equally applicable to other classes of geometries. The method can be used for both internal and external flow configurations, the only constraint being that the body geometries be specified in two-dimensional cross-sections stationed along the longitudinal axis of the configuration. Techniques for controlling various grid parameters, e.g., clustering and orthogonality are described. Techniques for treating problems arising in algebraic grid generation for geometries with sharp corners are addressed. A set of representative grid systems generated by this method is included. Results of flow computations using these grids are presented for validation of the effectiveness of the method.

Introduction

Numerical solution of field problems in any discipline, e.g., fluid dynamics, heat transfer, structures etc., requires a spatial discretization of the physical domain; that is, the generation of an organized set of points on the domain of interest for subsequent numerical solution of the governing equations. In the recent past numerous methods for generating grid-systems have been developed. These procedures compete with each other in their relative abilities to produce improved grid qualities such as smoothness of point distribution, clustering of points in regions of physical interest, ability to accommodate arbitrary boundary geometries, etc. A dominating philosophy in the realm of grid generation has been the introduction of a boundary conforming coordinate system[1] wherein coordinate lines are made coincident with physical boundaries thereby simplifying the application of finite - difference methods and eliminating the need for special procedures at the boundaries. Such systems allow transformation of the complex physical region into a uniform square mesh which simplifies coding at the cost of transformation of the governing equations

The methods for grid generation in current use fall chiefly in two broad categories: those employing partial differential equations and those constructing grids by algebraic means. The method to be described here is an algebraic procedure to be used in generating grids for finite-volume methods. It should be made clear at the outset that the present grid system is boundary-fitted only in that after spatial discretization segments of the physical boundaries form sides of the computational cells on the boundaries. The finite-volume method diseretizes the computational region into hexahedrons bounded by

quadrilateral planes. Thus, elemental volumes are bounded by flux surfaces and adjacent volumes share flux surfaces. The flux surfaces and volumes are computed from the actual physical coordinates of their vertices and therefore, there is no need for the introduction of boundary conforming curvilinear coordinate systems, the rigor of transformation into a uniform cube and the accompanying transformations of the governing equations.

Algebraic grid generation procedures include such techniques as normalization of boundary curves, transfinite interpolation and the use of intermediate interpolating surfaces. An overview of algebraic techniques in current use has been given by Thompson in [2]. Algebraic techniques are attractive because they are fast, easy to implement and require no numerical solution of partial differential equations. On the other hand, algebraic methods generally lack the smoothness inherent in elliptic grid generations and are more sensitive to specified point distributions on the boundaries. Elliptic methods, however, are not entirely free from this sensitivity but are generally more tolerant of nonsmooth boundary data than algebraic methods. A method for preventing effects of boundary discontinuities from propagating infield will be described in a later section.

Methods for grid generation by algebraic transformations fall in two broad categories: (1) shearing transformations and (2) boundary value interpolations. The present method is closely related to the second class of methods. In methods using shearing transformations, the four sided region enclosed by two curves connecting two straight lines in the physical plane is transformed into a rectangle by simply normalizing the coordinates. The points are distributed along the straight boundaries in the transformed rectangle according to a specified stretching function in order to obtain desired concentration of points. Clustering of points on the boundary is necessary in nonsmooth regions to prevent inward propagation of this lack of smoothness. In the boundary value interpolation technique a function on a region is found by interpolation between functions specified on the region boundaries. This technique is generally termed transfinite interpolation; blending function and connecting function interpolations being synonyms for the method. This procedure was used by Smith[3] to generate grids for wing-fuselage combinations using linear blending functions. A detailed description of transfinite interpolation has been given by Gordon and Hall[4]. Parameterization of the boundary curves should be carefully specified in order to avoid overlapping of grid lines. This method is more sensitive than partial differential equation methods to boundary point distributions. The blending functions may be polynomials whose arguments are expressed in terms of the curvilinear coordinates through stretching functions. An alternative way is to design the blending functions themselves to achieve the desired concentration of lines as in Eriksson[5] and Rizzi and Eriksson[6], where exponential functions are used. Grids generated algebraically in two-dimensional planes can be stacked to produce three-dimensional systems as in the present method. Such stackings may not in all cases produce sufficient smoothness in the direction of stacking. The present method provides for three-dimensional interpolation if desired. Application of transfinite interpolation in three-dimensions has been given by

Anderson and Spratley[7]. Eiseman[8] has applied the interpolation to a vector field of tangents in a multisurface transformation instead of the coordinate vectors. The tangents are defined on successive selected surfaces by the vector differences between positions. The interpolant creates a smooth vector field of tangents to the lines connecting the successive selected surfaces and the boundaries. The multisurface method has been extended in Eiseman and Smith[9] to use piecewise linear local interpolants in place of polynomials to provide local control over the coordinates. The controls may be used for example, to restrict the inward propagation of boundary slope discontinuities or to embed general rectilinear Cartesian systems within a global system while maintaining continuous first derivatives.

The present method generates a quasi-three-dimensional grid system by means of a homotopic blending between inner and outer surfaces. The method was originally developed for blended wing-body geometries that were generated by a semi-analytic procedure. A method was developed by Barger[10] for designing blended wing-body configurations with cross-sections that vary smoothly from a initial prescribed nose shape to a prescribed base shape such that the cross-sectional areas conform to a preassigned axial area distribution. The two end cross-sections are specified by the designer and the intermediate cross-sections are computed at specified stations along the axis of the body by interpolation using blending functions. Grids are then generated in two-dimensional planes located at each of these stations. The method in its essence consists of finding a family of transition curves by blending between two parametrically represented boundaries. The inner boundary is the body surface and the outer boundary is specified according to the needs of the particular problem. If the configuration resides within a duct, e.g., a wind tunnel test section, the duct wall serves as the outer boundary, otherwise a circular or elliptic outer boundary is chosen. The grid points in space are obtained by interpolation and blending functions which depend on the boundary data. The scheme is devised from an extension of the homotopic procedure used to design the body surface itself. This basic procedure has been previously applied by Moitra[11,12] to generate grids for blended wing-body geometries. The two dimensional grids are finally connected in the body axis direction. The outer boundary shape is represented as a transition surface with the same distribution of parameter values as are used to describe the inner surface. In case of a nonanalytically generated body surface the discrete points can be parameterized with respect to some chosen quantity such as angular location, arc length, etc, thus making the method applicable to a general class of body geometries.

The application of the homotopic blending method to grid-generation was treated quite briefly in reference 10. Only one example was given for a quasi-three-dimensional grid, and one for a fully three-dimensional grid. In view of this cursory treatment the purpose of the present paper is to pursue this subject in a greater depth and, in particular, to study the manner in which grid orthogonality at boundaries can be treated in the context of the homotopic blending theory.

Theory And Mathematical Development

Algebraic schemes are known to provide the fastest and the least expensive ways to generate grid systems. The method used in this study is an algebraic scheme devised to generate body geometries as well as the associated grid systems which has been applied to blended wing-body geometries, fighter aircraft configurations and certain internal flow geometries. The method for grid generation is a natural extension of that for defining the body surface and will be better understood if viewed in conjunction with the body geometry generation scheme.

Surface Equations: The problem of analytically designing a supersonic airplane or missile is generally influenced by two factors. One of these is the axial area distribution and the other is the cross-sectional shape, which except for axisymmetric missile bodies, varies from the nose to the base. Near the nose the cross-section is very often circular or nearly circular. Progressing along the longitudinal axis, the cross-section acquires various shapes as additional components such as canopies, wings, stabilizing surfaces are encountered. The same considerations as to shape variations are encountered in ducts and nozzles as well, since the inlet and exhaust cross-sectional shapes are usually different in realistic channel configurations.

A method has been developed[10] for designing body geometries with cross-sections that vary smoothly from an initial prescribed nose shape to a prescribed base shape such that the cross-sectional areas conform to a pre-assigned axial area distribution. The essential elements of the method are presented in the present paper. The body geometry may be defined as a surface component such that it varies gradually and smoothly between specified initial and terminal cross-sectional shapes. The surface component may represent a forebody, a wing-fuselage combination or a duct. The direction of variation is chosen to be the x-direction, i.e., the longitudinal axis of the configuration and the two end shapes are defined in y-z planes. The surface is generated by devising a way to vary the size as well as shape of the intermediate sections lying between the specified end shapes. The initial and terminal cross-sectional shapes are assumed to be represented in parametric form in terms of a parameter t. Let (y_{B1}, z_{B1}) and (y_{B2}, z_{B2}) denote the parametric representations of the initial and terminal shapes respectively, so that

at $x = x_1$

$$y_{B1} = y_{B1}(t)$$

$$z_{B1} = z_{B1}(t) \qquad t_a \le t \le t_b \qquad (1.a)$$

and at $x = x_2$

$$y_{B2} = y_{B2}(t)$$

$$z_{B2} = z_{B2}(t) \qquad (1.b)$$

on the same t domain (t_a, t_b)

The parameter t may be chosen to be the angular location, the arc length or any other appropriate quantity. The x variable is normalized by

$$x_n = \frac{x - x_1}{x_2 - x_1} \tag{2}$$

and an analytical blending function $C_n(x_n)$ is defined so that C_n varies smoothly from 0 to 1 as x_n varies from x_1 to x_2. The C is defined as

$$\begin{aligned} C(x) &= C_n[x_n(x)] \\ C(x_1) &= 0 \\ \text{and} \quad C(x_2) &= 1 \end{aligned} \tag{3}$$

The blending function C is smooth and monotonic. A transition surface representing a smooth blending of the two end shapes is given by

$$\begin{aligned} y(x,t) &= [1 - C(x)]y_{B1}(t) + C(x)y_{B2}(t) \\ z(x,t) &= [1 - C(x)]z_{B1}(t) + C(x)z_{B2}(t) \end{aligned} \tag{4}$$

To be general, the scheme must also have a provision for size variation of the intermediate sections in addition to the shape blending already attained. An independent scaling function $\lambda(x)$ is introduced to achieve the size variation of the blended surface. The scaling function is designed to be smooth and nonnegative, but not strictly monotonic. The resulting scaled surface is defined by the equations:

$$\begin{aligned} y(x,t) &= \lambda(x)\left\{[1 - C(x)]y_{B1}(t) + C(x)y_{B2}(t)\right\} \\ z(x,t) &= \lambda(x)\left\{[1 - C(x)]z_{B1}(t) + C(x)z_{B2}(t)\right\} \end{aligned} \tag{5}$$

More complex forms of transition surfaces may be obtained by choosing different blending functions and size scaling parameters. The vector form of the surface equation is

$$\bar{r}(x,t) = x\hat{i} + y(x,t)\hat{j} + z(x,t)\hat{k} \tag{6}$$

If the cross-sections are appropriately represented in polar form, then

$$y_{B1} = f_1(\varphi)\cos\varphi$$

(7)

$$z_{B1} = f_1(\varphi)\sin\varphi$$
$$0 \le \varphi \le 2\pi$$

with similar expressions for y_{B2} and z_{B2}. A variation of the transition surface is given by

$$y(x,\varphi) = \lambda y_{B1}^{(1 - C)} . y_{B2}^{C}$$
$$z(x,\varphi) = \lambda z_{B1}^{(1 - C)} . z_{B2}^{C} \qquad (8)$$

where C and λ are functions of x, and y_{B1}, z_{B1}, y_{B2}, z_{B2} are functions of φ. The transition surface in cylindrical coordinate is given by

$$\bar{x}(x,\varphi) = \lambda(x)\left[R_1(\varphi)\right]^{[1 - C(x)]} . \left[R_2(\varphi)\right]^{C(x)} \qquad (9)$$

assuming that R_1 and R_2 are the polar representation of the end sections.

The technique gives the user a large degree of control over the particular geometry to be generated. A base shape with sharp wing-body junctions causes no difficulty in generating a smoothly varying intermediate geometry. A judiciously chosen distribution of the parameter φ in any cross-sectional plane allows circumferential clustering of points in regions of geometrical interest, such as sharp corners, thus ensuring proper definition of complex body geometries, while a properly chosen transition function C(x) serves the same purpose in the axial direction. An appropriate distribution of x values serves to cluster grid planes along the axis of the configuration. This procedure guarantees a smooth transition from the initial to the base shape while maintaining a specified area distribution. The two end shapes are specified in a fashion that ensures a natural one-to-one correspondence with respect to the t-parameter values. This correspondence is valid at every intermediate section throughout the transition and precludes the possibility of t = constant lines developing waviness or crossing each other. The surface definition equations(eqs (5) - (9)) were developed by Barger[10] for numerically generating aerodynamic surfaces. Once the end shapes are specified by the designer, the intermediate sections may be computed and displayed graphically. The shape and scale functions C(x) and λ can be varied interactively until a desired transition surface is obtained. A schematic representation of the body definition procedure is presented in Figure 1. The prescribed shapes were a smooth circular shape at the nose S1, and a base shape S2 containing the central body and the trailing edges of the wing of a blended wing-body configuration. All the intermediate shapes, S3, S4, etc., were generated by blending between S1 and S2.

It should be noted that if the end shapes are difficult to describe analytically it may be necessary to represent them numerically by means of digitized data. For those cases the data may need to be smoothed by b-splines. Similarly, the functions controlling shape and size variations C(x) and λ respectively may be numerically specified; however, since these are normally smooth variations for aerodynamic shapes of interest, analytic expressions usually suffice for their representation.

Grid Generation: A simple extension of the homotopic procedure for generating the body surface itself results in a scheme for gridding the external field. The (x,t) coordinate lines defining the body surface form a natural surface grid. For calculation of supersonic flow over such a surface a quasi-three-dimensional grid system is sufficient. The external field-grid is generated by finding a family of transitional curves between the body surface as the inner boundary and a prescribed outer boundary. The outer boundary is represented as a transition surface with the same distribution of x and t values as are used to describe the inner surface. In case of nonanalytic body geometries the discrete data defining the surface may be parameterized with respect to some convenient quantity such as angular location, arc length, etc. in each two-dimensional cross-section. The grid is generated by defining at each x-station a homotopic variation from the inner surface $S_i(y_i,z_i)$ to the outer boundary $S_o(y_o,z_o)$. Denoting this homotopic parameter by η, and the shape transition function between the boundaries by C^*, we have,

$$\begin{aligned} C^*(\eta) &= 0, \qquad \eta = 0 \\ C^*(\eta) &= 1, \qquad \eta = 1 \end{aligned} \tag{10}$$

This function is taken to be independent of x; it retains the same value at each x-station. Essentially, the family of transition curves define a family of maps given by the homotopy

$$\left\{ h_\eta : A \rightarrow B \mid \eta \in I \right\} \tag{11}$$

where I is the unit interval [0,1]. The inner and the outer boundaries S_i and S_o are two homotopic maps such that

$$\begin{aligned} h_0 &= S_i \\ h_1 &= S_o \end{aligned} \tag{12}$$

and

Next, the size variation function for the grid lines is denoted by λ^* so that

$$\lambda_i < \lambda^* < \lambda_o \tag{13}$$

where λ_i and λ_o are the scaling functions used to generate the inner and the outer boundaries respectively. Since the size of the inner surface and possibly the outer surface vary with x, λ^* is not independent of x. It is expressed in terms of the normalized function $\tilde{\lambda}$ by

$$\lambda^* = \lambda_i + \tilde{\lambda}(\lambda_o - \lambda_i) \tag{14}$$

so that

$$\begin{aligned} \tilde{\lambda}(\eta) &= 0, \qquad \eta = 0 \\ \tilde{\lambda}(\eta) &= 1, \qquad \eta = 1 \end{aligned} \tag{15}$$

and $\tilde{\lambda}$ is independent of x.

The grid is defined at each x-station in terms of the function $C^*(\eta)$ and $\tilde{\lambda}(\eta)$, and a natural correspondence is established between the grid points at the various x-stations. Smooth variations of the inner and outer boundaries with respect to x will result in smoothly varying grid lines in the x-direction. Appropriate choices for the function $C^*(\eta)$ and the distribution of η result in approximate orthogonality of grid lines at the physical boundaries and clustering of grid lines near boundaries. The body-definition scheme is logically suggestive of a possible procedure for grid generation based on similar considerations of blending between an inner and an outer boundary. Finding a family of transition curves spanning the region between the boundaries consequently becomes the ideal procedure for generating the computational grid. A detailed description of the procedure follows.

Coordinates of each boundary are expressed in terms of a parameter τ. For the inner boundary

$$\begin{aligned} y_i &= y_i(\tau) \\ z_i &= z_i(\tau) \end{aligned} \tag{16}$$

while identical expressions denote the outer boundary. In polar coordinates τ could represent the angular coordinate. If z can be expressed as a single-valued function of y, then $\tau = y$. For shapes of greater complexity the choice of variables will vary. The procedure for grid generation consists mainly of determining a family of curves representing a gradual transition from the given inner boundary (y_i,z_i) to the outer boundary(y_o,z_o) in two-dimensional planes at each x-station. Assuming that the body surface coordinates have been

generated, a distribution of η values is specified. The η-distribution may be specified by means of polynomials, exponents, trigonometric functions etc., while ensuring that $\eta = 0$ on the body surface curve and $\eta = 1$ on the outer boundary. The shape transition function C^* for the grid is then specified by

$$C^*(\eta) = 1 - \eta^m \tag{17}$$

where m is a positive exponent that provides for additional control over line spacing near boundaries. Thus $C^* = 1$ on the inner boundary and $C^* = 0$ on the outer boundary with smoothly varying values distributed between boundaries. An arithmetic averaging between the boundaries yields the simplest family of grid lines given by

$$\begin{aligned} y(\eta,\tau) &= C^*(\eta)y_i(\tau) + [1 - C^*(\eta)]\, y_o(\tau) \\ z(\eta,\tau) &= C^*(\eta)z_i(\tau) + [1 - C^*(\eta)]z_o(\tau) \end{aligned} \tag{18}$$

where $0 \le \eta \le 1$

For complex boundaries, e.g, those involving corners, a geometric averaging yields smoother transition curves given by

$$\begin{aligned} y(\eta,\tau) &= y_i(\tau)^{C^*(\eta)} . y_o(\tau)^{[1 - C^*(\eta)} \\ z(\eta,\tau) &= z_i(\tau)^{C^*(\eta)} . z_o(\tau)^{[1 - C^*(\eta)]} \end{aligned} \tag{19}$$

The similarity with the scheme for body surface generation is clearly evident. Essentially $C^*(\eta)$ serves a purpose identical to that of $C(x)$ in the body-generation scheme. Here C^* provides for smooth blending between the shapes of the inner and the outer boundaries. Particular constant values of the η-parameter generate specific curves of the family described by equations (18) or (19) and a pre-chosen distribution of η determines the spacing of the resulting set of curves in each cross-sectional plane.

A major advantage of the present procedure derives from the fact that it allows an integration of the procedures for body and grid generation provided the body cross-sectional shapes are definable by analytical means. For body geometries available as discrete sets of points only the grid-generation part is of interest. If the parameters t and τ are chosen to be identical, e.g., the angular coordinate in both cases, then the body and the grid are definable by the same set of equations. It should be noted that the choice of the interpolation scheme, i.e.,

arithmetic averaging or geometric averaging for body definition and grid generation can be made independently of each other even though the extent of complexity of the body geometry usually has some influence on the choice of the blending technique for the grid. The final equations for generating y and z values for the entire field are found by combining equation (5) or (8) with equation (18) or (19). The four possible sets of grid-generation equations are given below.

1) Arithmetic averaging in body definition and geometric averaging in grid generation(equations (5) and (19)):

$$y(x,\tau,C,C^*,\eta) = \lambda^*(x)[\lambda(x)\{[1 - C(x)]y_{B1}(\tau) + C(x)y_{B2}(\tau)\}]^{C^*(\eta)} \cdot [y_o(x,\tau)]^{(1 - C^*(\eta))} \tag{20}$$

$$z(x,\tau,C,C^*,\eta) = \lambda^*(x)[\lambda(x)\{[1 - C(x)]z_{B1}(\tau) + C(x)z_{B2}(\tau)\}]^{C^*(\eta)} \cdot [z_o(x,\tau)]^{(1 - C^*(\eta))}$$

2) Arithmetic averaging in body definition and arithmetic averaging in grid generation (equations (5) and (18)):

$$y(x,\tau,C,C^*,\eta) = \lambda^*(x)[[\lambda(x)\{[1 - C(x)]y_{B1}(\tau) + C(x)y_{B2}(\tau)\}]C^*(\eta) + [y_o(x,\tau)][1 - C^*(\eta)]] \tag{21}$$

$$z(x,\tau,C,C^*,\eta) = \lambda^*(x)[[\lambda(x)\{[1 - C(x)]z_{B1}(\tau) + C(x)z_{B2}(\tau)\}]C^*(\eta) + [z_o(x,\tau)][1 - C^*(\eta)]]$$

3) Geometric averaging in body definition and geometric averaging in grid generation (equations (8) and (19)):

$$y(x,\tau,C,C^*,\eta) = \lambda^*(x)[\lambda(x)y_{B1}(\tau)^{(1 - C(x))} \cdot y_{B2}(\tau)^{C(x)}]^{C^*(\eta)} \cdot [y_o(x,\tau)]^{(1 - C^*(\eta))} \tag{22}$$

$$z(x,\tau,C,C^*,\eta) = \lambda^*(x)[\lambda(x)z_{B1}(\tau)^{(1 - C(x))} \cdot z_{B2}(\tau)^{C(x)}]^{C^*(\eta)} \cdot$$

$$[y_o(x,\tau)]^{(1 - C^*(\eta))}$$

4) Geometric averaging in body definition and arithmetic averaging in grid generation (equations (8) and (18)):

$$\begin{aligned} y(x,\tau,C,C^*,\eta) &= \lambda^*(x)[\{\lambda(x)y_{B1}(\tau)^{(1 - C(x))}.y_{B2}(\tau)^{C(x)}\}C^*(\eta) \\ &+ [y_o(x,\tau)[1 - C^*(\eta)]]] \\ z(x,\tau,C,C^*,\eta) &= \lambda^*(x)[\{\lambda(x)z_{B1}(\tau)^{(1 - C(x))}.z_{B2}(\tau)^{C(x)}\}C^*(\eta) \\ &+ [y_o(x,\tau)[1 - C^*(\eta)]]] \end{aligned} \tag{23}$$

The prescribed quantities are the nose and base shapes (y_{B1},z_{B1}) and (y_{B2},z_{B2}), respectively, and the outer boundary (y_o,z_o). All sets of curves including the body surface are then generated by a single set of equations. Therefore, at any given x-station, the body geometry and all curves between the inner and the outer boundaries are computed by a single procedure. This procedure is completed for each x-station. Spacing of the grid lines in all three coordinate directions can be controlled by choosing appropriate distributions of x,C,C^*,τ, and η. A schematic of the resulting quasi-three-dimensional grid system is presented in Figure 2.

Some flow situations might demand a truly three-dimensional grid and a quasi-three-dimensional system may not be adequate; for example, a modification of the basic grid generation scheme allows the development of a fully three-dimensional grid as follows. If the influence of the body shape is required to be felt upstream of the nose, the origin in the axial direction can be defined at an average x-station $\frac{x_1 + x_2}{2}$ along the axis of the body. Consequently the surface is now defined on the domain

$$-\varphi_{i,l} \le \varphi \le \varphi_{i,l} \tag{24}$$

while the t-domain remains unchanged

$$-1 \le t \le 1$$

The normalized outer boundary shape is defined to be an appropriate convex surface on the same φ , t domain with identical distribution of the φ and t variables as were used for the inner boundary. This normalized surface $r(\varphi,t)$ is multiplied by a large scale factor λ_o to determine the final outer boundary. A grid homotopy parameter η and a shape transition function $C^*(\eta)$ are defined as

done previously. The size transition function is denoted by $\lambda^*(\eta)$ such that $1 < \lambda^* < \lambda_o$ Additionally a homotopic function $\beta(\varphi)$ is defined such that β varies monotonically from 0 to 1 as $|\varphi|$ varies from 0 to 1. In the resulting scheme the grid-point locations are given by the following set of equations.

$$\begin{aligned} x(\varphi,\eta) &= \lambda^*(\eta)\beta(\varphi) \\ y(\varphi,t,\eta) &= \lambda^*(\eta)\{C^*(\eta)y_i(\varphi,t) + [1 - C^*(\eta)]y_o(\eta,t)\} \\ z(\varphi,t,\eta) &= \lambda^*(\eta)\{C^*(\eta)z_i(\varphi,t) + [1 - C^*(\eta)]z_o(\eta,t)\} \end{aligned} \tag{25}$$

where (y_i,z_i) and (y_o,z_o) denote the inner and outer boundary points respectively.

An alternative way is to input different distributions for the x-values for the inner and the outer boundaries. Let us denote these distributions by $x_i(I)$ and $x_o(I)$ where I denotes the I^{th} cross-sectional station. At each I-station a scale factor λ_o is defined such that

$$\lambda_o = \frac{x_o}{x_i} \tag{26}$$

Then a distribution for size transition $\lambda_x^*(I)$ is defined for x-values of grid points so that $1 < \lambda_x^* < \lambda_o$. A blending equation for the x-coordinates of grid-points is then included in the set of grid generation equations. The x-values are generated by

$$x(I,\eta) = \lambda_x^*(I,\eta)\{C^*(\eta)x_i(I) + [1 - C^*(\eta)]x_o(I)\} \tag{27}$$

Similar to the quasi-three-dimensional case, independent manipulation of the shape and size variation functions and η-distribution provide considerable control over grid characteristics such as orthogonality, clustering etc.

Generation of a grid around even simple wing-body configurations is by no means a simple task. The difficulties inherent in obtaining numerical solutions on a space discretized by a grid results in very demanding requirements for the grid generator that is expected to provide an optimum resolution with a minimum number of node points. It has been aptly pointed out by Eriksson[13] that the two chief components of computational fluid dynamics: grid generation and flow solution, should ideally be distinct operations and should be treated in

independent and modular ways. The method for grid generation should in no way be dictated by the particularities of a procedure for flow solution, and the flow solver should be able to accept as input an arbitrary set of points defining a grid and carry out solution of the governing equations thereon. In cases of practical interest, however, these two operations are intrinsically connected through such factors as data-structure, location and shape of boundaries and topology of the computational space. The present method of constructing three-dimensional grids for complex configurations is a homotopic blending procedure conceptually akin to transfinite interpolation and is attuned to the needs of finite-volume Euler flow solvers. This method generates grids by direct algebraic interpolation and not through algebraic transformation which is the norm with most transfinite methods in current use. A finite volume flow solver requires the physical coordinates of the grid points as input and transformation of the physical space into a cube in computational space is not imperative as would be in the case of finite difference algorithms. In the present procedure stretching transformations are replaced by stretching functions embedded in the blending functions of the interpolation methods to provide control of the point spacing. This homotopic scheme is transfinite, transformational logistic differences notwithstanding, in that it involves interpolation between functions specified along curves or surfaces rather than among point values and therefore, matches the functions at a nondenumerable set of points, although in practical situations these functions may be defined by discrete sets of values.

The present technique, being an algebraic procedure , is fast and allows explicit control of grid point-distribution. The approach is particularly well-suited for use in conjunction with interactive graphics. Human intervention in the control process of grid generation will remain indispensable until the advent of techniques that are truly coupled with the equations of motion and grid control is entirely adaptive. With interactive graphics this intervention can be instantaneous since algebraic grid generation methods are explicit and require relatively few computations. Grids may be generated, viewed and revised until a satisfactory grid is obtained in a reasonably short period of time.

Orthogonality

Introduction

Orthogonality of coordinate lines is a very desirable property of any grid system to be used in solving partial differential equations. Strict orthogonality is not an absolute necessity although excessive departures from it will result in deterioration of the numerical solution. Substantial deviations from orthogonality, however, are allowed by various flow solver algorithms. It may be prudent to point out that in the framework of general transformed computational spaces and finite difference procedures the use of strictly orthogonal systems allows the simplification of the transformed partial differential equations by dropping the terms in derivative transformations arising out of nonorthogonality, but the solutions can be substantially contaminated if any departure from true orthogonality should appear anywhere in the grid. In contradistinction to this the

retention of the full transformed equations and the use of a nearly orthogonal grid system in finite difference schemes has the advantage of introducing no numerical errors due to lack of orthogonality. The present grid generation scheme was developed particularly for use with finite-volume solutions, and since finite-volume solutions in physical space can be shown to be equivalent to finite-difference solutions in transformed space of the fluid dynamic equations in strong conservation form [14], it follows that near orthogonality in physical space is sufficient. Therefore, the terms orthogonality and near-orthogonality are considered synonymous in the present report.

Methods currently in use for generating nearly orthogonal grids are generally based on the principle of adjusting an existing non orthogonal grid. The methods use various approaches such as grid generation by partial differential equations, conformal transformations and construction of orthogonal trajectories. As mentioned before, the resulting systems are not sufficiently orthogonal to allow dropping of the terms arising out of nonorthogonality in derivative transformations.

Near orthogonality in P.D.E. grids is usually achieved by determination of orthogonal control functions. Elliptic generating systems produce coordinates that are more nearly orthogonal than those produced by most algebraic systems. The generating system of equations most often used is the Poisson system given by

$$\xi_{xx} + \xi_{yy} = P(\xi,\eta)$$
$$\eta_{xx} + \eta_{yy} = Q(\xi,\eta) \qquad (28)$$

where P and Q are functions used to provide grid control. Thompson, et al[15] incorporated exponential control functions in P which were used by Steger and Sorenson[16] to consider iterative determination of constants involved in order to achieve orthogonality at the boundaries. A different approach was taken by Visbal[17] to generate nearly orthogonal coordinate systems for simply connected regions employing the general generating equations for orthogonal systems by computing the control functions P and Q from a preliminary sparse grid.

Attainment of orthogonality at the boundaries while preserving conformality is generally not considered a viable proposition. Moretti[18] has advocated the use of a sequence of elementary transformations e.g., Karman-Trefftz, Joukowski, bilinear, etc.. in succession to map an arbitrary curve to a near circle. Finally a shearing transformation may be used to map the near circle into a rectangle. The grid so obtained is expected to be nearly orthogonal. Sockol[19] has used two conformal mappings followed by a numerical grid generation to generate nearly orthogonal grids for cascades. More recently, Ives[20] has applied conformal techniques to a three-dimensional configuration involving an inlet center body combination. In this procedure a conformal mapping is used in two coordinate directions and the distribution in the third

direction is produced by algebraic stretching.The resulting three-dimensional grid is orthogonal in two directions.

Methods based on the construction of orthogonal trajectories are particularly well suited to orthogonalization of an originally nonorthogonal grid. These methods have an advantage over methods designed to produce orthogonal systems directly in that they allow easier control over line distribution. Since one family of lines from an originally nonorthogonal system is retained, the methods provide greater flexibility in generating a final orthogonal system with desired line distribution.

A procedure for construction of grids by orthogonal trajectories has been applied by Graves[21] and Graves and Hamilton[22]. In this procedure, curves of a nonorthogonal system are first generated by any chosen distribution function along straight lines connecting points on the inner and outer boundary curves. Orthogonal trejectories are then constructed by the following steps: (1) Intersection of the normals at selected points on the inner boundary with the next curve outward are located: (2) The normal directions at the intersection points are determined and new intersection points using these new normal directions are located; and (3) final points on the outer curve are then chosen to be midway between the corresponding pairs of intersection points. This procedure is applied successively between each pair of curves of the original system. The points determined by the above procedure are then connected by straight line segments to generate the final grid. The resulting lines will not be strictly orthogonal to either the inner or the outer boundary but the departure from orthogonality will be small. In a related procedure Ghia et al.[23], determined points on successive curves of a nonorthogonal grid such that the orthogonality condition

$$g_{ij} = 0 \qquad i \neq j$$

is satisfied. This procedure produces grids qualitatively similar to grids generated by the method of Graves. The initial nonorthogonal grid may be generated in a variety of ways, however, algebraic transformations are preferred for this purpose over other means because of the explicit and continuous definition of the transformations provided by algebraic methods. Shearing, Hermite or multisurface transformations are adequate for this purpose. A natural correspondence between the orthogonal trajectories and images of characteristic curves under the given nonothogonal transformation has been given by Eiseman and Erlebacher[24]. A general development of this topic has been presented by Eiseman[25].

It is generally held that algebraic procedures for grid generation, unlike P.D.E. systems have no inherent mechanism for producing orthogonal grids and simultaneously maintaining smoothness and even when methods, such as the ones described above, are used to achieve near-orthogonality, intersection of grid lines of the same family is an often unavoidable problem. In this paper a theoretical development and a method will be presented that exploits the pseudo differential nature of homotopic procedures to produce grids that mimic

P.D.E. grids with reasonable closeness so far as grid qualities e.g., orthogonality, smoothness and non-intersection of grid lines are concerned.

Present Method:

Understanding of the present method for achieving near orthogonality and smoothness from homotopic procedures will be facilitated by a review of the basic tenets of homotopy theory that play important roles in the development of the theory. Given $X \subset R^k$, let $Xx[0,1]$ denote the subset of R^{k+1} consisting of all (x,t) with $x \in X$ and $0 \leq t \leq 1$. Then two mappings

$$f, g : X \rightarrow Y \tag{29}$$

are called smoothly homotopic if there exists a smooth map

$$F : X x[0, 1] \rightarrow Y \tag{30}$$

with

$$\begin{aligned} F(x,o) &= f(x) \\ F(x,1) &= g(x) \end{aligned} \tag{31}$$

where t denotes the homotopy parameter.

Many of the properties of a map are not altered if the map is deformed in a smooth manner. Intuitively, a smooth map $f : X \rightarrow Y$ is a deformation of another $f_o : X \rightarrow Y$ if they may be joined by a smoothly evolving family of maps.$f_t : X \rightarrow Y$ In the present method of grid construction equations (18) or (19) may be seen to be algebraic representations of the homotopic family t_{η_i} that smoothly maps the inner boundary into the outer boundary through the homotopy parameter η that varies between 0 and 1 from one boundary to the other. Homotopy is an equivalence relation on smooth maps from x to y. In order to recover the smoothly evolving family of maps joining f_o and f_1 one defines.

$$f_t : X \rightarrow Y \quad \text{by} \quad f_t(x) = F(x,t) \tag{32}$$

where $F(x,t)$ can be specified algebraically.

It is assumed that f_t is a diffeomorphism. A function f is a diffeomorphism if f^{-1} exists and both Df and Df^{-1} exist and are continuous. This assumption is not restrictive and has the following consequences.

(i) $f_t(x) = f_t(y)$ if and only if $x = y$, hence trajectories are uniquely specified by their initial conditions.

(ii) The derivative of a trajectory with respect to the initial condition exists and is non singular.

Consequence i) may be seen as a statement of one-to-one correspondence. Both consequences are automatically satisfied by choosing F to be an explicitly specified algebraic relation.

It can be shown[26] that diffeomorphisms constitute a stable class of smooth maps of a compact manifold x into a manifold y .The present method of attaining orthogonality through homotopies is based on the concept of stability of maps. From a point of view of practicality and physical measurements no continuous functional relationship is ever perfectly determined over a wide range of argument values. Consequently, the properties of a mapping that are of physical relevance are only those which remain valid when the map is subjected to slight deformations. Such properties are termed "stable" properties, and the collection of maps that possess a particular stable property may be referred to as a stable class of maps. In essence, a property is stable provided that whenever f_o: x - y possesses the property and f_t: x - y is a homotopy of f_o, then for some $\varepsilon > 0$, each f_t with $t < \varepsilon$ also possesses the property. Thus small perturbations in the homotopy parameter do not alter the stable properties of a map.

Here we are concerned with the orthogonality of the trajectories joining corresponding points on the successive curves, specially at the given boundaries. In this context a few stability considerations are particularly important. The properties of grid smoothness and conformity of the overall grid with the given boundaries are stable under slight deformations of the map. The property that a curve pass through a given point is not stable, since a small change in the homotopy parameter can immediately distort any such curve to avoid the point,(Fig. 3). It may be seen therefore, that the points on a curve may be redistributed by judicious choice of the homotopic parameter distribution in order to achieve a desired set of trajectories. The points on the boundaries are of course fixed and not altered by these changes. Another property of interest is that of intersection of curves. The naive point-set condition of intersection is seldom stable. and therefore, is meaningless in the physical world. Nontransversal intersection, however, is physically relevant in the present context , and this property can be readily seen (Fig. 4) to be unstable. Two curves of the family that intersect at an even number of points may be separated by adjusting the distribution of the homotopy parameter. These properties considered together suggest the possibility of generating approximate orthogonal trajectories while preventing intersection of curves of the same family by choosing appropriate distributions of the homotopy parameter. These particular distributions can be determined from the boundary conditions. In figures 5.a and 5.b a family of curves before and after small perturbations in the homotopy parameters for achieving near-orthogonality of the trajectories, are

presented schematically. The perturbations redistribute the points lying on each curve so that the trajectories joining them become orthogonal.

The problem of intersecting trajectories is presented graphically in figure 6. For extreme cases of boundary curves with sufficient concavity, an attempt to orthogonalize the trajectories may result in intersecting trajectories. In Figure 6.a, two such trajectories emanating from the concave region of the boundary are seen to intersect at a pair of points. In the enlarged view presented in Figure 6.b the two trajectories are seen to intersect at the points A and B. The curve f_b lying between the points of intersection is seen to locally turn back on itself. An arbitrary curve of the family, f_p, may now be imagined, which intersects the curve f_b at two points. The problem of intersection of the trajectories at points A and B may thus be translated to the intersection of two curves of the same family f at points P and Q as seen in Fig 6.c. As mentioned before, this type of intersection is an unstable property of the map. The homotopy parameter b may therefore be locally adjusted to force f_b completely clear of f_p thus removing the problem of intersecting trajectories. The present procedure for generating near-orthogonal grids while preventing grid line intersections does not necessitate generating a non-orthogonal grid first and then adjusting this preliminary grid. The controlling values and distributions of the homotopy parameter are derived from the boundary data and used directly to generate the final grid. This capability of generating orthogonal grids is inherent in the homotopy procedure in much the same way as the method of orthogonal control functions is inherent to the P.D.E grid generation systems. It may be noted that the relation of smooth homotopy is an equivalence relation and consequently transitive [27]. This method of constructing orthogonal grids by homotopy is therefore equally applicable to the multisurface procedure. The algebraic description of the homotopy method of orthogonal grid construction follows.

The basic interpolation scheme, equations (18) may be re written as

$$\begin{aligned} x &= x_i E + x_o(1 - E) \\ y &= y_i E + y_o(1 - E) \end{aligned} \tag{33}$$

where $$E = 1 - \eta^m \tag{34}$$

The subscripts i and o denote the inner and the outer boundaries respectively. Here E varies between 1 at the inner boundary and 0 at the outerboundary and plays a role analogous to that of a homotopy parameter. Modifications of E, therefore, causes slight deformations of a given map and may be used to achieve orthogonality. It can be seen that E serves as a parameter that propagates the influence of the inner boundary on the coordinates of any point in the field. In order to achieve orthogonality of the trajectories at the inner boundary the influence of the inner boundary on points near it needs to be increased. Here, this control is provided through the use of an exponent P. The coordinates x and y of any point in the field may then be modified by

$$x = x_i E^P + x_o(1 - E^P)$$

$$y = y_i E^P + y_o(1 - E^P) \qquad (35)$$

$$P < 1.0$$

The exponent P is not a constant and must be determined from the boundary data subject to the orthogonality condition. Two kinds of segments of the inner boundary that need to be considered separately are a) those that are nearly horizontal and b) those that are nearly vertical. For nearly horizontal segments, orthogonality at the boundary may be obtained by modifying the x-coordinate of the point on the curve lying next to the boundary as shown in Figure 7.a. In nearly vertical segments a modification of the y coordinate achieves the same effect. (Fig 7.b). The exponent P for any trajectory is determined from the condition that two vectors be orthogonal. One of these vectors is found by connecting the point(x_i,y_i) on the inner boundary and the point (x,y) lying just off the boundary on the trajectory in question (Fig. 8). The other vector passes through the print (x_i,y_i) and a point (x',y') on the line passing through (x_i,y_i) and parallel to the line joining (x_{i+1},y_{i+1}) and (x_{i-1},y_{i-1}) on the inner boundary. These two vectors are denoted by A and B respectively. The method for evaluating P for the two kinds of inner boundary segments are presented below.

a) **Nearly horizontal segments**

As mentioned before only the x coordinate needs to be adjusted for trajectories emanating from inner boundary segments that are nearly horizontal. The orthogonality condition is that the dot product of the vectors A and B be zero, i.e.,

$$A.B = 0 \qquad (36)$$

which translates into

$$(x - x_i)(x' - x_i) + (y - y_i)(y' - y_i) = 0 \qquad (37)$$

Substituting

$$x = x_i E^P + (1 - E^P)X_o \qquad (38)$$

and $y = y_i E + (1 - E)y_o$

one obtains

$$(x_o - x_i)(i - E^P)(x' - x_i) + (y_o - y_i)(1 - E)(y' - y_i) \qquad (39)$$

Rearranging terms results in

$$E^P = 1 + A(1 - E) \tag{40}$$

where

$$A = \frac{(y_o - y_i)(y' - y_i)}{(x_o - x_i)(x' - x_i)} \tag{41}$$

Finally solving for P one yields

$$P = \frac{\ln(1 + A(1 - E))}{\ln E} \tag{42}$$

where E has the value corresponding to the homotopic curve lying next to the inner boundary. The value of P given by equation(42); will result in near orthogonality between the trajectory emanating from (x_i,y_i) and the inner boundary.

b) **Nearly Vertical Segments**

For boundary segments that are nearly vertical it is necessary to adjust the y coordinate values for points on the trajectory. The values of x and y are then given by

$$\begin{aligned} x &= x_i E + (1 - E)x_o \\ y &= y_i E^P + (1 - E^P)y_o \end{aligned} \tag{43}$$

substitution of (43) in the orthogonality requirement

$$A.B = 0$$

results in

$$(E - 1)(x_i - x_o)(x' - x_i) + (E^P - 1)(y_i - y_o)(y' - y_i) \tag{44}$$

Rearrangement of terms yields

$$E^P = 1 + B(1 - E) \tag{45}$$

where

$$B = \frac{(x_i - x_o)(x' - x_i)}{(y_i - y_o)(y' - y_i)} \qquad (46)$$

The final solution for P is

$$P = \frac{\ln(1 + (1 - E)B)}{\ln E} \qquad (47)$$

The value of P given by (47) will result in near orthogonality of trajectories emanating from nearly vertical segments of the inner boundary. A logical switch from scheme a to scheme b depending on the nature of the boundary segment can be easily implemented.

The problem of grid lines or trajectories intersecting each other in the interior of the field is considered next. As seen above the use of the exponent P derived from the orthogonality condition ensures orthogonality at the physical boundary. Intersecting trajectories can be separated by modifying P. This may be achieved by the use of an exponent q such that

$$x = x_i E^{P^q} + x_o(1 - E^{P^q}) \qquad q < 1.0 \qquad (48)$$

Raising P to the power q increases the value of the exponent of E, which in turn makes the grid lines follow the inner boundary less closely and reduces the chance of trajectory intersection. Using a constant value for q, however, will reduce orthogonality. In order to maintain orthogonality near the boundary the logical solution is to cause q to decay as one proceeds outwards from the inner boundary along trajectories. This is achieved by making q a function of E such that

$$q = F(E) \qquad (49)$$

where

$q = 1$ at the inner boundary

and $q = 0$ at the outer boundary.

The use of equation (48) with q defined as in (49) will preserve grid orthogonality in the region close to the boundary while preventing grid line intersection away from the boundary.

To assist in following the train of logic involved in this procedure of successive exponentiation a formal logic proof of the concept follows. The region of interest is understood to be the region near the inner boundary where orthogonality is required. The predicates O and C represent grid orthogonality and grid line intersection respectively and P,Q and Q_e denote the acts of using the exponent

P, raising P to a constant exponent q, and making q a function of E in that order. In the following table the procedures of exponentiation, their formal logic representation and comments explaining the consequences are given.

Procedure	Formal Logic	Comments
E^P	$P \Rightarrow O$ (1)	Raising E to the power of P as in equation (35) produces orthogonality near the boundary while trajectories may or may not intersect
$E^{P^q}/_{q=\text{const}}$	$Q \Rightarrow {}'(O \wedge C)$ $\Rightarrow {}'O \vee {}'C$ (Demorgan's Law) $\Rightarrow {}'P \vee {}'C$ (2) (from (1))	Raising P to the constant power q will remove grid line intersection at the cost of orthogonality, i.e., will prevent the construction of grids that are orthogonal and contain grid intersection.
$E^{P^q}/_{q=f(E)}$	$Q_e \Rightarrow P \wedge Q$ $\Rightarrow P \wedge ({}'P \vee {}'C)$ from (2) $\Rightarrow (P \wedge {}'P) \vee (P \wedge {}'C)$ (Laws of distributivity of conjunction with respect to disjunction) [$(P \wedge {}'P)$ is an absurdity] $\Rightarrow P \wedge {}'C$ $\Rightarrow O \wedge {}'C$ (3)	Use of q = f(E) preserves P near the boundary while maintaining the effects of Q in the inner field. Result (3) shows that the use of q = f(E) produces orthogonality and eliminates grid line crossings.

The procedure described above produces smooth grids that are nearly orthogonal near the inner boundary and do not contain intersecting grid lines. The procedure is simple since all blending and control functions are specified explicitly. As opposed to other methods of grid construction by orthogonal trajectories, it is not necessary to generate a preliminary nonorthogonal grid and later adjust it. All exponents and coefficients are derived from the boundary data and applied explicitly to generate the final grid in one execution of the procedure.

Description of the algorithm

The algorithm is structured to produce nearly orthogonal, smooth grids for any arbitrary three dimensional configuration. The configuration geometry is assumed to be available in the form of two-dimensional curves in planes stationed along the longitudinal axis of the body(see Fig. 1). Required inputs are the the shape functions defining these cross-sectional shapes, factors governing their size variations, the shape of the outer far-field boundary and an optional file containing the discrete point-set representation of the body geometry. Brief discussions on important parts of the algorithm follow.

Body surface definition

a) Analytic Case:

Blending between two prescribed end shapes is performed to generate all intermediate sectional shapes. Equation (5) defines the transition surface shown schematically in Figure 9, in terms of the end shape functions and two coefficients, each defined as a function of a single independent variable. The two end shapes (YB1,ZB1) and (YB2,ZB2) depend only on t, whereas the shape variation function c and the size variation function λ depend only on x. The normalized end shape cross-sections are specified by defining the functions $F_i(t)$ and $G_i(t)$, where

$$\begin{aligned} F_1(t) &= ZB1(t) \\ G_1(t) &= YB1(t) \\ F_2(t) &= ZB2(t) \\ G_2(t) &= YB2(t) \end{aligned} \qquad (50)$$

and t is a circumferential parameter with a chosen distribution, which varies from -1 to +1 from one wing tip to another. The functions $G_i(t)$ are usually set to have the corresponding t-values, i.e.

$$\begin{aligned} G_1(t) &= t \\ G_2(t) &= t \end{aligned} \qquad (51)$$

while $F_1(t)$ and $F_2(t)$ can be specified by any chosen algebraic formulae. F_1 and F_2 are usually given separately for the upper and lower surfaces of the configuration; however, care must be exercised to ensure that they match at appropriate points such as wing tips and wing-body junctions. The normalized cross-section at the nose of the configuration is usually an ellipse or a circle as schematically shown in Figure 10.a. The terminal cross-section typically contains a circular central body and the trailing edges of the wings as represented in Figure 10.b. Once the end shapes have been determined, a

normalized sectional shape at station x along the longitudinal axis is computed by combining the F_1 and F_2 shapes as follows,

$$\begin{aligned} FI &= C(x)F_1 + [1 - C(x)]F_2 \\ GI &= C(x)G_1 + [1 - C(x)]G_2 \end{aligned} \qquad (52)$$

where C(x) is any function of x that equals 1 at x_n and 0 at x_f. The distribution of C(x) determines the nature of the blending between the two terminal shapes. The scaled cross-section at station x is then determined by multiplying the coordinates (FI,GI) at x by a scale function SC(x), which is normally zero at the nose(x_n), and given a specified size at the base at x_f. The final coordinates of the configuration surface (YI,ZI) are then given by the following equations:

$$\begin{aligned} YI &= SC(x)\{C(x)G_1 + [\,1 - C(x)]G_2\} \\ ZI &= SC(x)\{C(x)F_1 + [\,1 - C(x)]F_2\} \end{aligned} \qquad (53)$$

b) **Discrete Case:**

In the event that the surface geometry is not defined by analytic means, the geometry may be input to the code as an ordered set of discrete points. The input file must contain the grid points defining the cross-section in each axial plane in succession. Moreover, the number of discrete points in each plane must remain constant in order to ensure continuous surface grid lines.

Grid generations:

A normalized shape for the outer boundary is first prescribed through the shape functions $F_3(t)$ and $G_3(t)$. The function F_3 is specified as an algebraic relation defining a desired curve, e.g., a circle, and $G_3(t)$ is set equal to t as in the case of the configurations end sections. The shape of the outer boundary may be varied from one x-station to another by making F_3 a function of x. A schematic representation of the outer boundary shape appears in Figure 11. Once the outer boundary has been specified at each station, a set of grid lines is calculated in each plane by blending between the inner and outer boundaries through the parameter η using equations(18). A distribution of η -values along trajectories is first chosen and then the distribution of the grid lines is determined by the function $E(\eta)$ where

$E(\eta) = C^*(\eta)$ as defined in equation (17) , where

$E(\eta)$ must be 1 when $\eta = 0$ and 0 for $\eta = 1$. In order to ensure near orthogonality at the boundary and nonintersection of trajectories, the coefficient P of $E(\eta)$ has to be determined from equations (42) or (47) depending on whether the inner boundary is locally nearly horizontal or vertical. For this purpose a test on the

local slope of the inner boundary is performed. If the absolute value of the slope exceeds a preset limit the surface is considered nearly vertical and nearly horizontal otherwise. The actual scaled size of the outer boundary is defined by the multiplication factor SCL3. Consequently, the set of transition grid lines from the inner surface(SC.FI,SC.GI) to the outer grid boundary. (SCL3.F_3, SCL3.G_3) is given by

$$Z = E.SC.FI + (1 - E).SCL3.F3$$
$$Y = E.SC.GI + (1 - E).SCL3.G3 \qquad (54)$$

where Z,Y are the final coordinates of the points in the field. Thus the parameters controlling the grid are x,t and E whose distribution may be varied as desired. The shape of the body can be changed by varying the end-shapes

$F_1(t)$, $G_1(t)$
$F_2(t)$, $G_2(t)$

and the shape transition and scale functions

C(x)
SC(x)

while $F_3(t)$, $G_3(t)$ determine the shape of the grid.

The generated grid points are saved in a file for graphics post-processing or for use by a flow-solver code. A detailed description of the computer code for grid generation can be found in a companion report[28].

Examples of generated body geometries and grid systems

A representative spectrum of body geometries and coordinate grid systems produced by the theory and numerical procedures described in the previous sections will next be presented. The versatility of the method is manifested in the presented examples. The effects on the body surface shape and grid control, of the various parameters, coefficients and functions used in the theory are illustrated. Computed grid examples include those for analytically defined body geometries as well as ones for body geometries represented by discrete point sets.

Body geometries:

A set of four body geometries generated by the method of blending between prescribed nose and base shapes are presented. For each case the shape transition, the scaling factors and their effects on the resulting body shape are explained. All of these geometries were generated using equations(5) of the body definition scheme.

Body 1. A three-view representation of this configuration is given in Figure 12. The frames are appropriately labeled with the coordinate directions. The xy frame contains the planform shape, the xz frame represents the side elevation and the front projection appears in the yz plane. The configuration was generated by specifying elliptic shapes for both the nose and base cross-sections. The final configuration has elliptic cross-sections at each x-station with the major and minor axes in a ratio of 1:0.18. The shape transition function C(x) and the scaling function $\lambda(x)$ used for this configuration are defined as

$$C(x) = 1.0$$

$$\lambda(x) = \frac{x(12.0 - x)}{20.0} \tag{55}$$

Setting C(x) equal to the constant value of unity throughout has the effect of not altering the shapes of the intermediate cross-sections at all, so that if the end shapes are elliptic the intermediate cross-sections are strictly elliptic also. The specified function of the scaling factor produces the curved outer edges appearing in the planform and the side elevation.

Body 2. This configuration represents a spiked fore body with small canard surfaces. The nose shape is specified to be a very small circle and the base shape contains a circular central body and the straight line edges of the canard surfaces. The intermediate cross-sections gradually change in shape from the nose to the base as determined by the shape transition function C(x) and the scale factor $\lambda(x)$. The function C(x) is given by

$$C(x) = \left(\frac{x_f - x}{x_f - x_n}\right)^{1.7} \tag{56}$$

where x_n and x_f are the x values at the nose and the base, respectively.

Two different distributions are used for the scaling factor $\lambda(x)$, one for x values lying between X_n and one-third of the length of the configuration and another for the rest of the length. The distributions are given by

$$\lambda(x) = \lambda_n + (\lambda_{1/3} - 1)\frac{x}{x_{1/3}} \quad x \le x_{1/3}$$

$$\lambda(x) = \lambda_{1/3} + (\lambda_f - \lambda_{1/3})\left[\frac{x - x_{1/3}}{x_f - x_{1/3}}\right] \quad x > x_{1/3} \tag{57}$$

where $x_{1/3}$ is the x-value for the point lying at one-third the length from the nose, and λ_n, λ_f and $\lambda_{1/3}$ are the prescribed scaling factor values at the nose, the base and at $x_{1/3}$ respectively.

Body 2. A blended wing-body configuration is shown in Figure 14. This geometry is representative of modern high-speed aerospace vehicles or missiles which are characterized by smooth blending of the wing into the fuselage. As in the previous case, the prescribed end shapes are a small circle at the nose and a circular fuselage and wing trailing edges at the base. In this case the shape transition function C(x) and the scaling factor $\lambda(x)$ are given by

$$C(x) = \left(\frac{x_f - x}{x_f - x_n}\right)^{1.7}$$

$$\lambda(x) = R^{0.8}.\lambda_f + (1 - R^{0.8})\lambda_n \qquad (58)$$

where $$R = \frac{x - x_n}{x_f - x_n}$$

The value of the function C(x) varies from 1 at the nose to 0 at the base and generates the intermediate cross-section shapes by a smooth blending between the two end shapes.

Body 4. This case illustrates the use of the scaling function $\lambda(x)$ to generate body shapes of varying complexity. The configuration presented in Figure 15 has the same nose and base shapes as the previous case but the scaling function has been modified to produce the interesting planform of the blended wing-body geometry. The shape transition function C(x) is identical as that used for body 3. The shape controlling functions for this configuration are

$$C(x) = \left(\frac{x_f - x}{x_f - x_n}\right)^{1.7} \qquad (59)$$

and $$\lambda(x) = Q + 0.15\,\mathrm{Sin}\left[\left(\frac{x - x_n}{x_{1/3}}\right)\pi\right] \qquad (60)$$

where $$Q = \left(\frac{\lambda_f - \lambda_n}{x_f - x_n}\right)(x - x_n) \qquad (61)$$

and $x_{1/3}$ has the same definition as given for body 2. The intermediate cross-sections are produced by a smooth blending between the end shapes while conforming to the size variation imposed by equation (60).

These examples demonstrate that independent control over the functions controlling the shape and size variations can be used to generate complex aerospace vehicle shapes for use in high-speed computations. The technique is particularly suitable for generating advanced body shapes having smooth wing-body junctions, i.e. blended wing-body geometries, that eliminate the strong shocks that would occur at sharp wing-body junctures.

Computed grid examples.

The homotopic scheme is applied to several examples in the present section. Grid configurations obtained using the basic scheme are presented first. The techniques for orthogonality and prevention of grid intersection are illustrated in the examples that follow. The body geometries for which grids were generated vary in complexity ranging from simple airfoils to blended wing-body geometries and fighter aircraft. For most cases only a part of the field near the inner body surface is presented for clarity. Relevant values of coefficients and parameter distributions are given for each example.

Basic grids.

The grid examples in this group, presented in Figures 16 to 25 were generated using equations 18. No special provisions for orthogonalization or prevention of crossing of grid lines were incorporated in these cases. The lines of the homotopy map were uniformly distributed between the inner and outer boundaries through the following distribution functions

$$\eta = \frac{K - 1}{N - 1} \tag{62}$$

and

$$C^{\bullet}(\eta) = 1 - \eta \tag{63}$$

where η is the homotopy parameter, N denotes the index of the outer boundary and K varies between 1 and N from the inner to the outer boundary.

The sectional planar grid shown in Figure 16, was generated for the elliptic body presented in figure 12. The outer boundary was prescribed to be flatter at the bottom in order to facilitate computation of high angle-of-attack flows. The smoothness of the transition of the lines of the map between the boundaries is apparent. The trajectories in this case are straight lines joining corresponding points on the inner and outer boundaries. Orthogonality was not imposed; however, the grid was found to be satisfactory for finite-volume computations at moderate Mach numbers. The orthogonalized grid for this configuration will be presented in a later set of results in this section. Sectional grids at two x-stations of the body geometry presented in Figure 14 are shown in figures 17 a and 17 b. The sections presented in figures 17 a and 17 b are located at the midlength of the body and near the base, respectively. A smooth family of curves is seen to have evolved in each case; moreover the discontinuity at the sharp wing tips does not propagate into the field as would be usually expected for algebraic

procedures. Similar plots of sectional grids for two sections of the body shown in Figure 15 are presented in Figures 18-a and 18-b.

The grid examples presented so far are illustrations of O-grid topologies in planes normal to the axis of the body and the direction of the flow. The next two examples are for C-grid topologies where the plane of the grid is parallel to the direction of the flow. A planer grid for a section of a semi-elliptic cylinder, typically representing the leading edge of a wing, is presented in Figure 19. The outer boundary is prescribed as a semi-circle of a chosen radius and the distribution of the family of curves is again specified to be uniform. A grid in a chord-wise plane of a supersonic wing is presented in Figure 20. The inner boundary in this case was specified by a discrete point set. The figure represents the region close to the airfoil and a smooth blending of the grid lines is evident. The grid lines have been distributed uniformly.

The quasi-three-dimensional grid generation technique is illustrated in Figures 21 a through 21 e for a typical fighter aircraft configuration. A planer grid for a section of the configuration containing the fuselage and a vertical stabilizer surface appears in Figure 21.a. Quasi-three-dimensional grid systems are constructed by generating a planer grid for each cross-section of the body and finally connecting the corresponding grid points on these planes in the body-axis direction producing a grid-system that completely envelopes the body. A cut-away view of the total grid system is shown in Figure 21.b. A portion of the outer boundary surface has been cut away to reveal the underlying grid structure. The grid system is presented for the left half of the configuration and five planer grids at different locations along the axis of the configuration are visible. The configuration with two planer grids appears in Figure 21.c. Enlarged views of these planer sections are presented in Figures 21.d and 21.e.

The next set of results will demonstrate the effects of grid-stretching, i.e., nonuniform distribution of the grid lines through control of the homotopic parameter η, and grid-clustering on the body surface by chosen distributions of the circumferential parameter t. Concentration of grid lines near the inner boundary is effected by prescribing values for the coefficient m in the definition of $C^*(\eta)$ in equation (17). It has been shown before that a value of unity generates uniformly distributed lines. The planar grids presented in figures 22.a and 22.b show grid line concentrations achieved by setting $m = 1.8$ and $m = 2.2$, respectively. Greater concentration of lines in the wall boundary regions is achieved by larger values of m. Similar plots for two sections of a blended wing-body configuration appear in Figures 23.a and 23.b. The chosen value for m is 2.0 for both sections, however, m may be specified as a function of x in order to achieve varying degrees of concentration in different sections. A comparison of Figure 23 with Figure 18 reveals the additional grid concentration near the inner surface. A sectional grid for an airfoil wing section appearing in Figure 24 shows grid lines concentrated near the wing surface using m=1.8.

Grid clustering at any location on the body surface can be achieved by prescribing a modified cosine distribution for the circumferential parameter t. In a given section t varies from -1 to +1 from one wing-tip to another. For bodies

with a plane of symmetry it is sufficient to specify the t-distribution on only one side of the plane of symmetry from this plane to the wing-tip, i.e., in the domain $0 \leq t \leq 1$. The following examples illustrate grid-clustering at various points on the body surface along with the t-distributions that generated the clustering. A sectional grid with grid lines clustered at the tips of a body with elliptic cross-section is presented in Figure 25. The distribution function for t in this case is given by,

$$A = -\cos\left[\frac{(J - 1)\pi}{(N - 1)}\right] \tag{63}$$

$$t = A^{(1 - A)} \tag{64}$$

where N is the total number of circumferential points on the surface in a given section and J varies from 1 to N circumferentially along the surface from one wing-tip to another. A similar distribution was used to cluster grid points at the wingtips of a blended wing-body configuration as shown in Figure 26. A modification of the exponent in equation (64) results in clustering near the plane of symmetry. The grid presented in Figure 27, showing clustering at the plane of symmetry was generated using

$$t = A^{(1.0 + F(1.0 - A))} \tag{65}$$

where A is given by equation (63) and the value of F determines the degree of clustering. Grid lines can be clustered near any point on the body surface denoted by $t = t_c$ by modifying the point distribution by the following equations.

$$t = A^{\left[P + Q\left(\frac{t - t_c}{1.0 - t_c}\right)\right]} \tag{66}$$

and

$$t = A^{\left[R + S\left(\frac{t_c - t}{t_c}\right)\right]} \tag{67}$$

where the constants P, Q, R and S are carefully chosen to provide desired clustering. The grid shown in Figure 28 was obtained by clustering near $t_c = 0.4$ for a section of a blended wing-body configuration. The values used for P,Q,R and S were 1.1, 1.2, 0.98 and 0.25 respectively.

The grid examples presented so far were produced with no efforts at orthogonalization. The following group of examples demonstrate the imposition of near orthogonality at the inner boundary by the use of equations (38) and (43) with the values of the exponent P given by equations (42) and (47). A sectional grid for a body with elliptic cross-section, with partial orthogonality of grid lines near the body surface is presented in Figure 29. An enlarged view of

the region near the inner surface appears in Figure 30. Grid lines are seen to start nearly orthogonal to the body surface and then gradually curve away toward their destination points on the outer boundary. Orthogonality of the trajectories is more clearly visible in the sectional grid for a blended-wing-body configuration presented in Figure 31. The scheme for orthogonalization automatically switches from equation (38) to equation (43) across the concave region at the wing-body function and the values of the coefficient P are determined according to the near horizontality or verticality of the inner boundary. The resulting trajectories are smooth and swerve away from the orthogonal direction as they approach the outer boundary. A close-up view of the inner region is presented in Figure 32. Although the previous two examples involve analytically defined body surfaces, the procedure for generating orthogonal trajectories is equally applicable to body geometries input as discrete point sets, as is shown in the next example in Figure 33. This configuration contains sharp wing-body junctions and sharp wing tips, and orthogonality has been imposed only on the outboard portion of the wing. The resulting grid lines are smooth and no special problems are caused by the sharp wing tip as seen in the enlarged view in Figure 34.The next example in Figure 35 is a C-type grid for a section of a supersonic wing. The wing surface was input via discrete point coordinates. Orthogonality of grid lines near the leading edge is clearly visible in the enlarged view in Figure 36.

As mentioned before, the use of the exponents P as defined by equations(42) and (47) ensures orthogonality, but not the prevention of grid lines of the same family from crossing each other. In body geometries involving sharp corners and concave regions the imposition of orthogonality at the surface causes grid lines to intersect within the grid field as shown in Figure 37. This problem occurs often in body geometries of realistic complexity and is usually untreatable by algebraic means. The homotopic procedure described here provides a way to maintain orthogonality at the inner boundary while preventing grid lines from crossing each other through the use of equation (48),where the coefficient q is defined by equation (49). The application of this procedure is demonstrated in the next few examples. The first example involves a blended wing-body configuration. A sectional grid generated with the orthogonality constraint imposed without the coefficient q results in the distorted grid shown in Figure 38. The orthogonal trajectories emanating from the concave wing-body junction region are seen to have intersected those from the wing surface. The trajectories are heavily constrained to follow the nearly orthogonal direction until the last point immediately before the outer boundary causing distortion and depletion over a large portion of the grid. The use of equation (48) with q defined by

$$q = 1.0 - \left[\frac{N - 2}{N_{out} - 2}\right]^k \qquad (68)$$

$$k < 1.0$$

resolves the problem of intersecting trajectories and generates the smooth grid shown in Figure 39, with orthogonality preserved near the inner boundary. The

coefficient K determines the rate of decay of orthogonality from the inner boundary to the outer boundary along trajectories. Values of K may be chosen to provide desired degrees of decay. The same principles are applied to the next case involving a blended wing-body-tail configuration. The basic orthogonlization scheme without the coefficient q, produces results similar to the previous example as shown in Figure 40. The strict adherence of the trajectories to the orthogonality constraint results in grid intersections and severe distortions over most of the surface. A smooth orthogonal grid shown in Figure 41 is obtained using equation (48) and (68) as in the previous example. It is important to note that any additional constraints, e.g., concentration of grid lines near the surface or grid clustering near a point on the surface are not altered by this orthogonalization procedure.

All the previous grid examples were for external flow configurations where the grid was generated between the body surface as the inner boundary and a far-field surface as the outer boundary. The grid-generation procedure is equally applicable to some internal flow configurations e.g., ducts and nozzles as will be demonstrated in the following set of grid examples. In internal flow geometries all or part of the nozzle wall is usually chosen as the outer boundary while a number of choices exist for treating the inner boundary. These choices lead to three basic topological arrangements for internal grids. All three types are illustrated in the examples to follow.

The first type of arrangement is very similar to a polar grid where the center-line of the nozzle is treated as the inner boundary and the nozzle wall serves as the outer boundary. A sectional grid with this arrangement is presented in Figure 42. The inner boundary collapses to a point on the center-line in the planar section but the grid is generated by a procedure identical with that used for external flow configurations. Stacking of such planar grids results in a singular line along the center of the nozzle which is easily treatable in finite-volume applications. It may be noted that concentration and clustering of grids are still achievable by the methods used in external grids.

The second type of grid arrangement has been applied to grid the exhaust from a blended wing-body aircraft in the region aft of the base as seen in Figure 43. An enlarged view is presented in Figure 44. In this arrangement the lateral diameter of the exhaust area is treated as the inner boundary and the upper and lower walls of the exhaust port is treated as outer boundaries. The grid is generated for the upper and lower halves of the region separately but complete continuity of the trajectories across the diameter is maintained. The trajectories are normal to the lateral diameter and the lines of the other family converge at the corner points fo the region at the ends of the diameter. In each sectional plane the trajectories of the internal grid match the external grid across the boundary of the internal grid. This is ensured by using the same distribution of points on this boundary when generating both the internal and external grids. A number of these sectional grids can be stacked behind the base of the body in order to study the flow in the wake region of the configuration. The blended wing-body configuration with four grids stacked in the wake region appears in Figure 45.

The third type of internal grids is different from the first two in that only a part of the duct wall is treated as the outer boundary. A sectional grid for a duct with circular cross-section is presented in Figure 46, in the left half plane. The grid is generated separately for the parts lying above and below the lateral diameter of the duct. The duct wall is considered in two parts. The part closer to the vertical diameter is chosen to be the outer boundary. The rest of the wall is treated as a side boundary. The distribution of points on the side boundary determines the distribution of the homotopy parameter η,used in blending. The Lateral diameter is treated as the inner boundary and continuity of the trajectories across it is maintained. This topological arrangement was employed to grid a duct with varying cross-sectional shapes. The duct shown in Figure 47, has cross-sections smoothly varying from a circle at one end to a narrow ellipse at the other end. The configuration with the sectional grids is presented in Figure 48. A smooth variation of the cross-sectional shapes ensures smooth grid lines in the longitudinal direction of the configuration and the resulting grid is suitable for computing internal flows in ducts.

Application to solution of the Euler equations.

In this section a sample set of results obtained by solving the Euler equations governing fluid flow is presented for a few configurations which were gridded by the procedure described in this report. All these results were obtained in the computational space discretized into hexahedral cells by a quasi-three-dimensional grid system created by stacking planar grids at stations along the longitudinal axis of the body. The Euler equations were solved on this discretized physical domain by a finite-volume algorithm with Runge-Kutta integration in time [11,12].

A plot of computed pressure contours in a sectional plane for a body with elliptic cross-sections at a Mach no of 1.6 and an angle of attack of 6^{0} degrees is presented in Figure 49. The resulting contours are smooth and important details, e.g., the shock lying below the body are seen to be effectively captured. Surface pressure values for a cross section of an elliptic body are plotted against angular location in Figure 50. The Mach number and the angle of attack for this case are 2.5 and 5 degrees respectively. A reasonably close agreement is noted between the computed values and the experimental results given by Allen et.al [29]. A much more complex structure of shocks and expansions is seen to have been captured in the sectional plot of computed pressure contours for a blended wing body configuration presented in Figure 51. The flow conditions for this case were $M = 3.0$ and $\alpha = 3.0$ degrees. Grids generated by the method described here are, therefore, seen to be suitable for use in computing high-speed flows for complex configurations. Computed pressure contours in the planform of a blended wing-body configuration appears in Figure 52. The shocks at the nose and the point where the wing begins to flare out are clearly seen to have been captured. The pressure contour lines are smooth in the longitudinal directions signifying that there is no severe distortion of grid cells in that direction. Finaliy, in Figure 53, a sectional plot of pressure

contours for a fighter aircraft-like configuration at M = 1.8 and $\alpha = 5^{0}$ reveals all the expected details near the wing tip and the wing-body junction.

Concluding remarks.

Algebraic grid generation schemes are the fastest and the most efficient procedures available for generating computational grids for general configurations, because of the fact that the interpolant functions are specified explicitly. Acute sensitivity to boundary point distribution and the propagation of boundary discontinuities to points infield are, however, problems that have plagued algebraic schemes. Previously these difficulties were overcome by clustering the boundary mesh points at points with slope discontinuity and local controls on the interpolants e.g., in multisurface transformations. These local controls are very much dependent on the particular configuration under consideration and apriori knowledge of the problem areas are usually necessary in formulating the control functions. In the present homotopic procedure the interpolants are modified by control of the homotopy parameter where the control functions are derived from the boundary data and play roles analogous to control functions in elliptic systems. This homotopic method prevents propagation of discontinuities and intersection of the trajectories while maintaining near orthogonality at the boundary. The resulting grids are smooth and have been successfully used in high-speed Euler computations.

All grid generation schemes, however complex, need some degree of human intervention in order to achieve grids with desired characteristics for sufficiently complex configurations. The human intervention is best implemented in interactive computer graphics environments; and algebraic schemes, by virtue of their speed, are ideally suited for this kind of applications. For a quasi-three-dimensional grid system, each planar grid can be viewed on a terminal and modified by changing the grid parameters if desired in a short amount of time provided the communication rate is sufficiently high. Problem areas can be identified by viewing grids with a small number of points thus further reducing development time.

References

1. Thompson, J. F., Thames, F. C. and Mastin, C. W., "Boundary-Fitted Curvilinear Coordinate Systems for Solution of Partial Differential Equations on Fields Containing Any Number of Arbitrary Two-Dimensional Bodies," NASA CR-2729, 1977.

2. Thompson, J. F., Warsi, Z. U. A. and Mastin, C. W., "Boundary-Fitted Coordinate Systems for Numerical Solution of Partial Differential Equations -A Review, " Journal of Computational Physics Vol. 47, 1982.

3. Smith, R. E., "Algebraic Grid Generation About Wing-Fuselage Bodies," 15th Congress of the International Council of the Aeronautical Sciences, Sept. 1986 London, U.K.

4. Gordon, W. J. and Hall, C. A., "Construction of Curvilinear Coordinate Systems and Applications to Mesh Generation," Int. J. Numer. Meth. Eng. Vol. 7, 1973, pp. 461.

5. Eriksson, L. E., "Three-Dimensional Spline-Generated Coordinate Transformations for Grids Around Wing-Body Configurations. Numerical Grid Generation Techniques," NASA CP-2166, 1980, pp. 253.

6 Rizzi, A. and Eriksson, L. E., "Transfinite Mesh Generation and Damped Euler Equation Algorithm for Transonic Flow Around Wing-Body Configurations," AIAA Computational Fluid Dynamics Conference, Palo Alto, CA, 1981.

7. Anderson P. G. and Spratey, L. W., "Finite Difference Grid Generation by Multivariate Blending Function Interpolation," NASA CP-2166, 1980, pp. 143.

8. Eiseman, P. R., "A Multi-Surface Method of Coordinate Generation," J. Comput. Phys. Vol. 33, 1979, pp. 118.

9. Eiseman P. R. and Smith, R. E., "Grid Generation Using Algebraic Techniques," NASA CP-2166, 1980, pp. 73.

10. Barger R. L. and Adams, M. S., "Semianalytic Modeling of Aerodynamic Shapes," NASA Technical Paper 2413, NASA Langley, April 1985.

11. Moitra, A., "Numerical Solution of the Euler Equations for High-Speed, Blended Wing-Body Configurations," AIAA Paper No. 85-0123, 1985

12. Moitra, A., "Euler Solutions for High-Speed Flow About Complex Three-Dimensional Configurations," AIAA Paper No. 86-0246, 1986.

13 Eriksson, L. E., "Generation of Boundary-Conforming Grids Around Wing-Body Configurations Using Transfinite Interpolation," AIAA Journal, Vol 20, No. 10., October 1982.

14. Thompkins, W. T. Jr., "Analysis of Pseudo-Time-Marching Schemes for Application of Turbomachinery Calculations," Recent Advances in Numerical Methods in Fluids: Advances in Computational Transonics, Vol. 4, edited by W. G. Habashi, Pineridge Press, 1985, pp 577-605.

15. Thompson, J. F. Thames, F. C. and Mastin, C. W., "'TOMCAT' -A Code for Numerical Generation of Boundary-Fitted Coordinate Systems on Fields Containing any Number of Arbitrary Two-Dimensional Bodies," Journal of Computational Physics, 1977, pp. 245.

16. Steger, J. L. and Sorenson, R. "Automatic Mesh-Point Clustering near a Boundary in Grid Generation with Elliptic Partial Differential Equations," Journal of Computational Physics, Vol. 33, 1979, pp. 405-416.

17. Visbal, M., "Generation of Nearly-Orthogonal Body-Fitted Coordinate Systems in Two-Dimensional Singly Connected Regions," M.S. Thesis, Rutgers University of NJ, 1980.

18. Moretti, G., "Grid Generation Using Classical Techniques," NASA CP-2166, 1980, pp. 1.

19. Sockol, P. M., "Generation of C-type Cascade Grids for Viscous Flow Computations," NASA CP-2166, 1980, pp. 437.

20. Ives, D. C. and Liutermoza, J. F., "Analysis of Transonic Cascade Flow Using Conformal Mapping and Relaxation Techniques," AIAA Journal, Vol. 15, 1977.

21. Graves, R. A., "A Simple Numerical Orthogonal Coordinate Generator for Fluid Dynamic Applications," NASA CP-2166, 1980, pp. 307.

22. Graves, R. A., and Hamilton, H. H., "Simple, Numerically Generated Orthogonal Coordinate System for Viscous Flow," AIAA Journal, Vol. 19, 1981,2 pp. 133.

23. Ghia, U., Hodge, J. K., and Hankay, W. L., "An Optimization Study for Generating Surface Oriented Coordinates for Arbitrary Bodies in High-Re Flow," AFFDL-TR-77-117, AirForce Flight Dynamics Lab. WPAFB, 1977.

24. Eiseman, P. R., and Erlebacher, G., "Grid Generation for the Solution of Partial Differential Equations," NASA Contractor Report 178365, August 1987.

25. Eiseman, P. R., "Orthogonal Grid Generation," Numerical Grid Generation, Ed by J. F. Thompson, North-Holland, 1982, pp. 447.

26. Guillemin, V., Pollack, A., "Differential Topology," Prentice-Hall, Inc., Englewood Cliffs, New Jersey, 1974.

27. Milnor, J. W., "Topology from the Differential Viewpoint," The University Press of Virginia, 1965.

28 Moitra, A., "HOMAR: A Computer Code for Generating Homotopic Grids Using Algebriac Relations. Users' Manual," NASA CR-4243, 1989.

29. Allen, J. M., Hernandez, G., Lamb, M., "Body Surface Pressure Data on Two Monoplane-Wing Missile Configurations with Elliptic Cross Sections at Mach 2.5," NASA TM-85645, Sept. 1983.

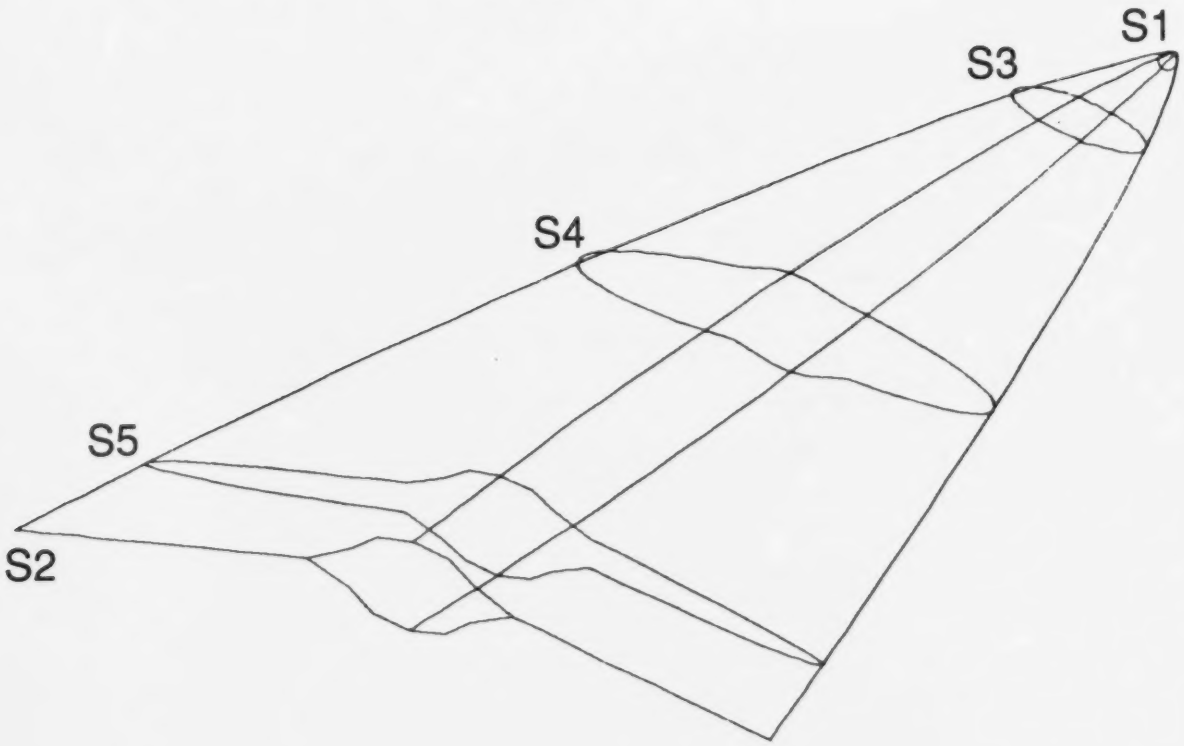

Figure 1 Schematic representation of body definition.

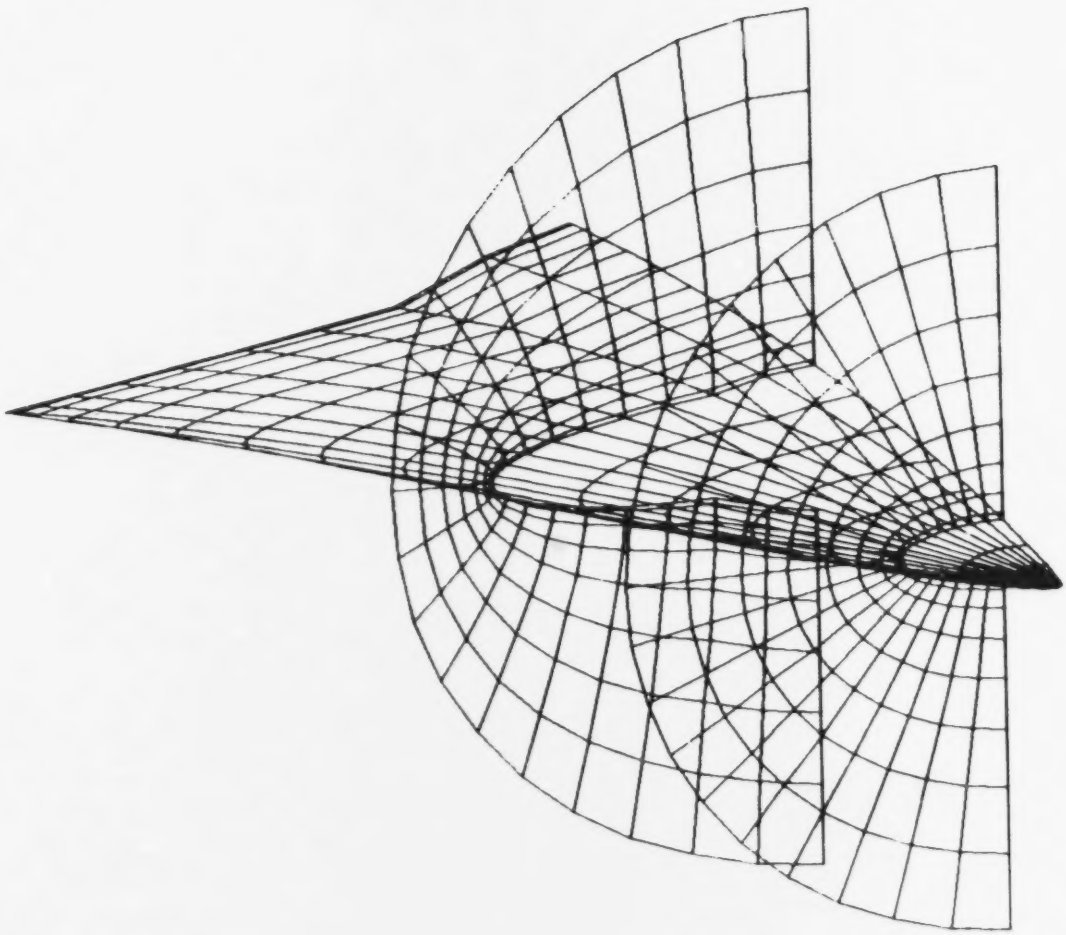

Figure 2 Schematic diagram of quasi-three-dimensional grid systems

Figure 3 Unstable property: Curve passing through given point.

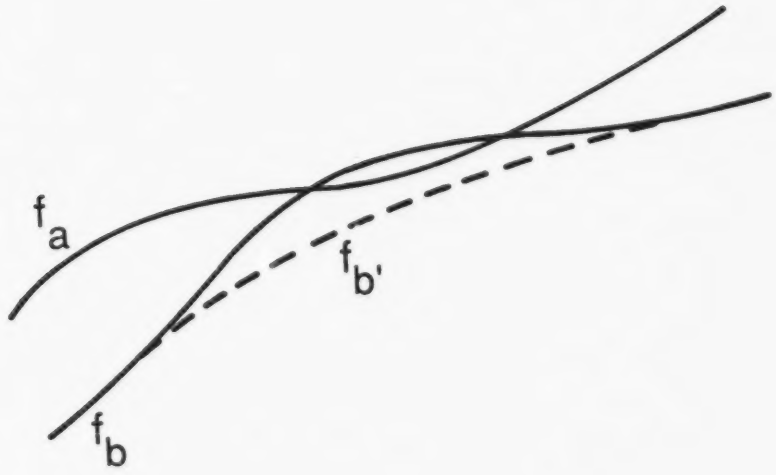

Figure 4 Unstable property: Nontransversal intersection.

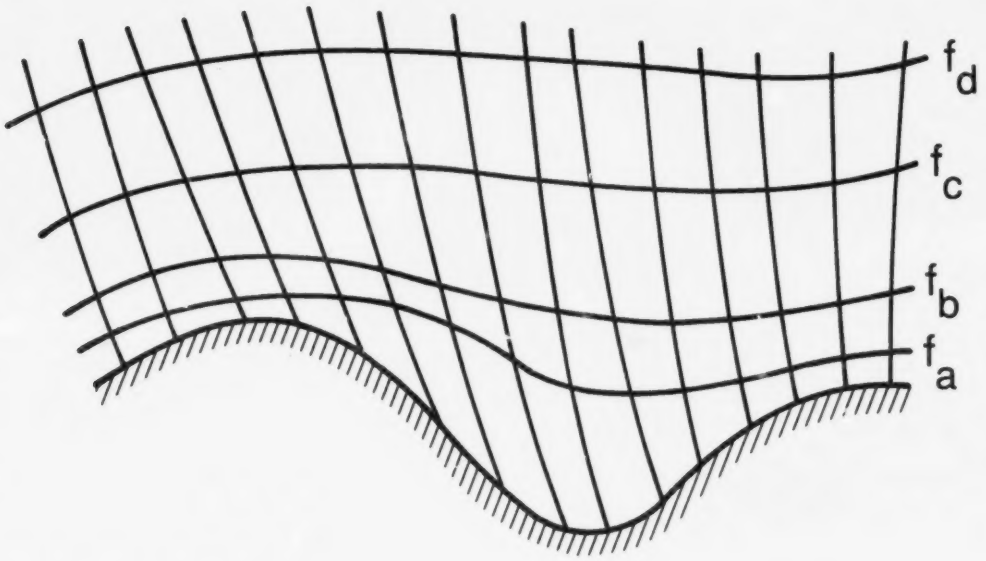

Figure 5.a Family of curves before perturbation.

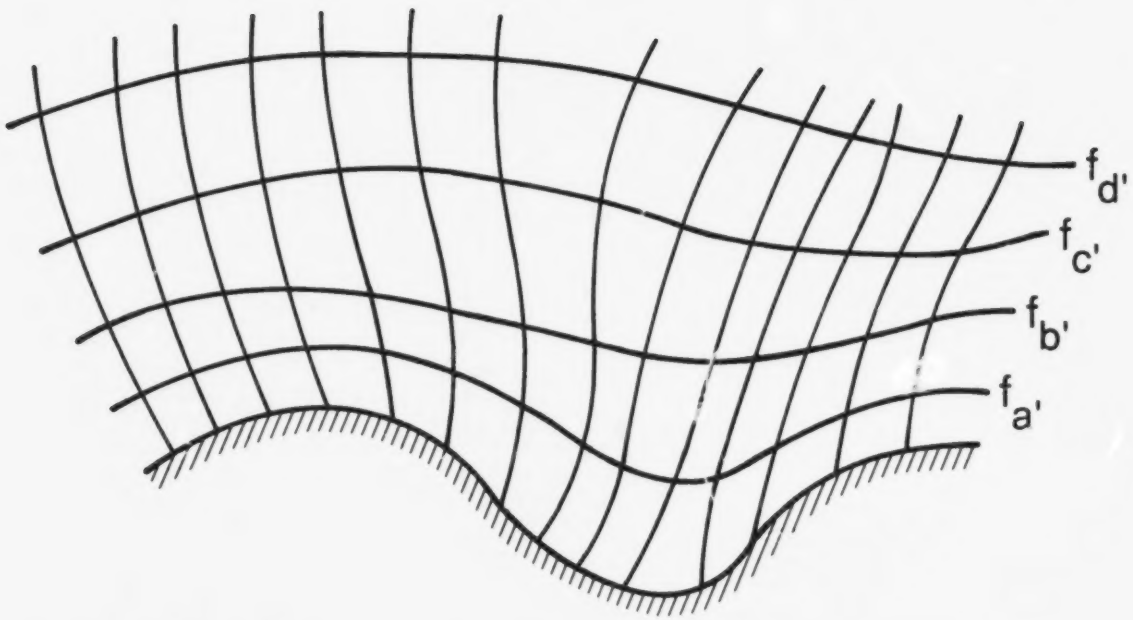

Figure 5.b Family of curves after perturbation.

Figure 5 Homotopic perturbation to achieve near-orthogonality.

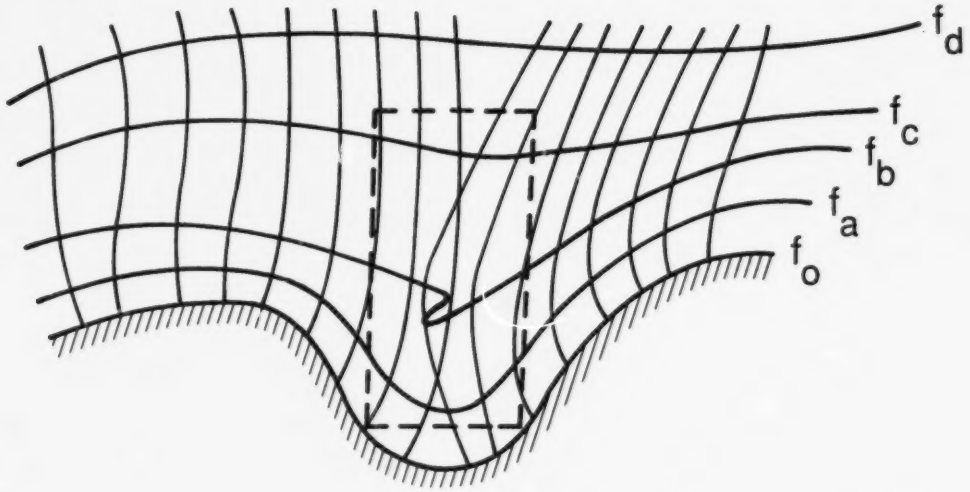

Figure 6.a Map with intersecting trajectories.

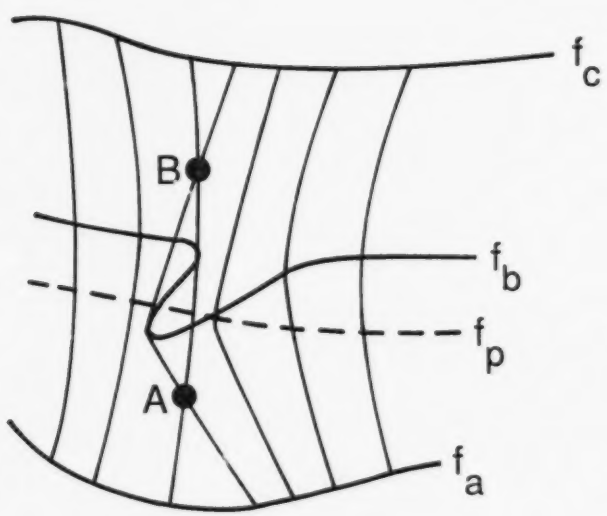

Figure 6.b Region of intersection.

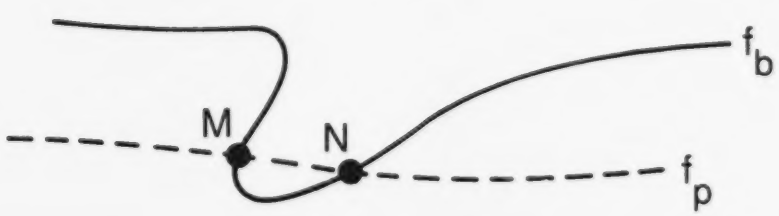

Figure 6.c Corresponding intersecting maps.

Figure 6 Intersection of orthogonal trajectories.

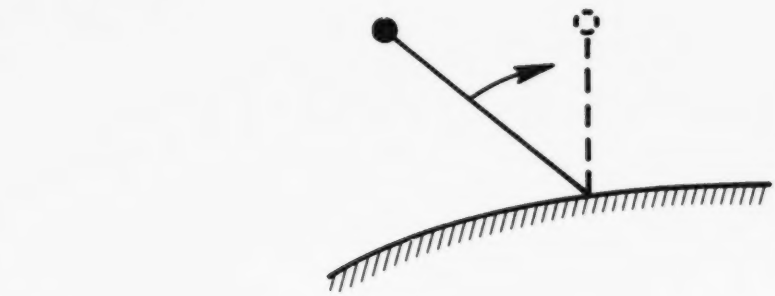

Figure 7.a
Modification of the x-coordinate for horizontal boundaries.

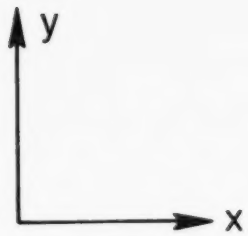

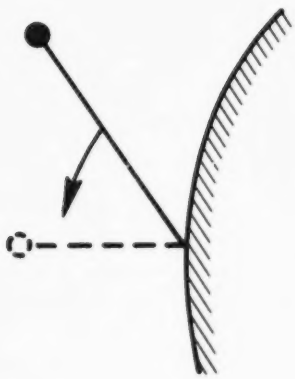

Figure 7.b Modification of the y-coordinate for vertical boundaries.

Figure 7 Modification of coordinates to achieve orthogonality at horizontal and vertical boundaries.

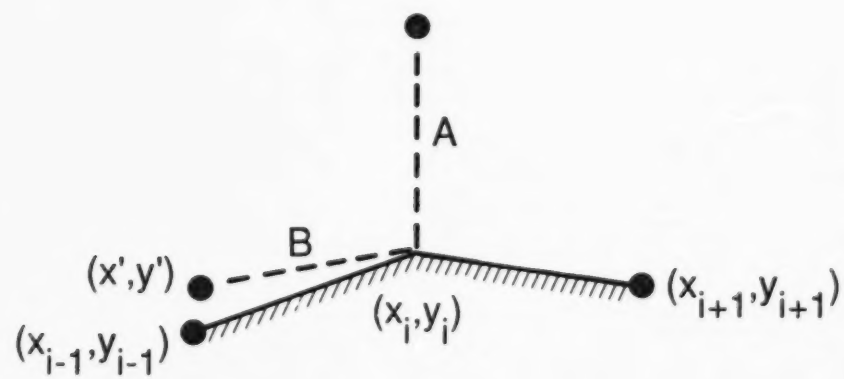

Figure 8 Vectors used in orthogonalization process.

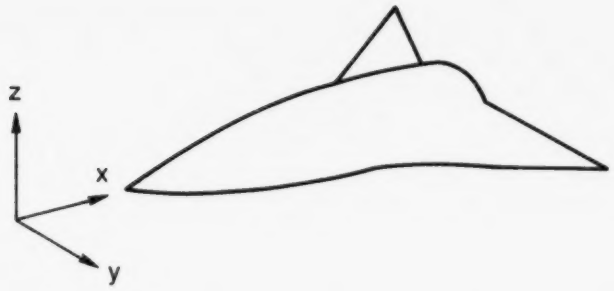

Figure 9 Body geometry defined as transition surface.

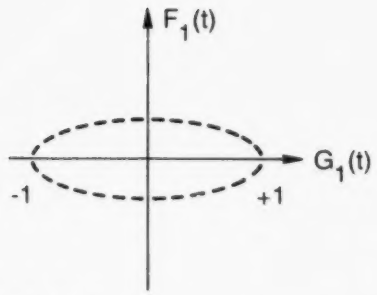

Figure 10.a

Normalized nose section at $X = X_N$.

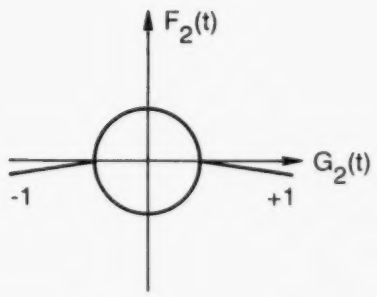

Figure 10.b

Normalized terminal section at $X = X_F$.

Figure 10 Normalized end shapes.

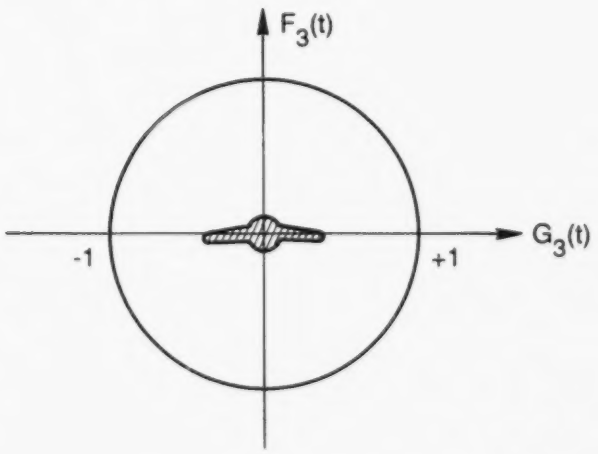

Figure 11 Normalized shape of grid outer boundary.

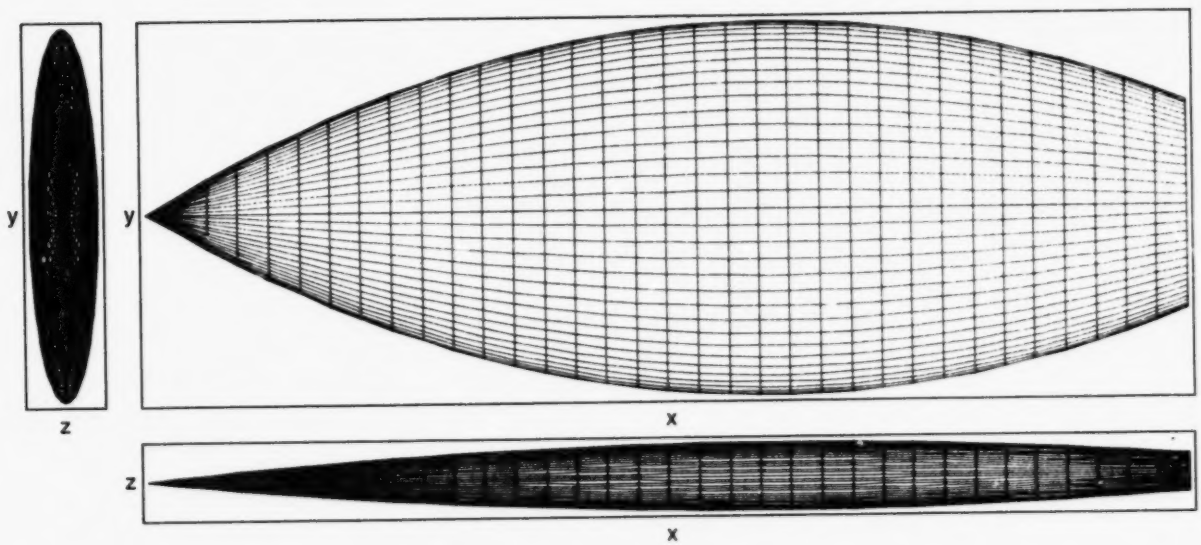

Figure 12 Three-view representation of body with elliptic cross-section.

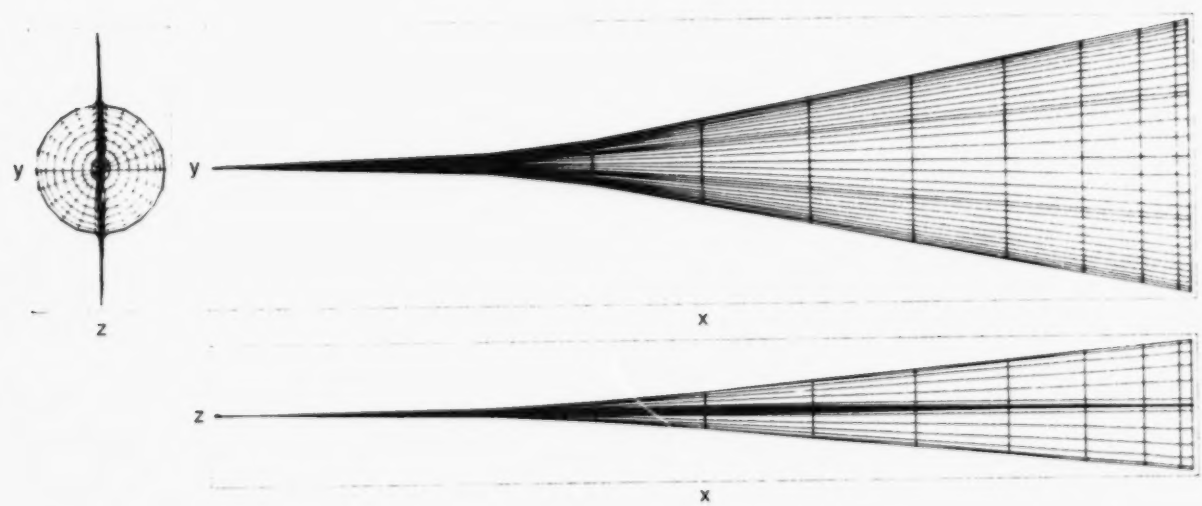

Figure 13 Three-view representation of spiked forebody.

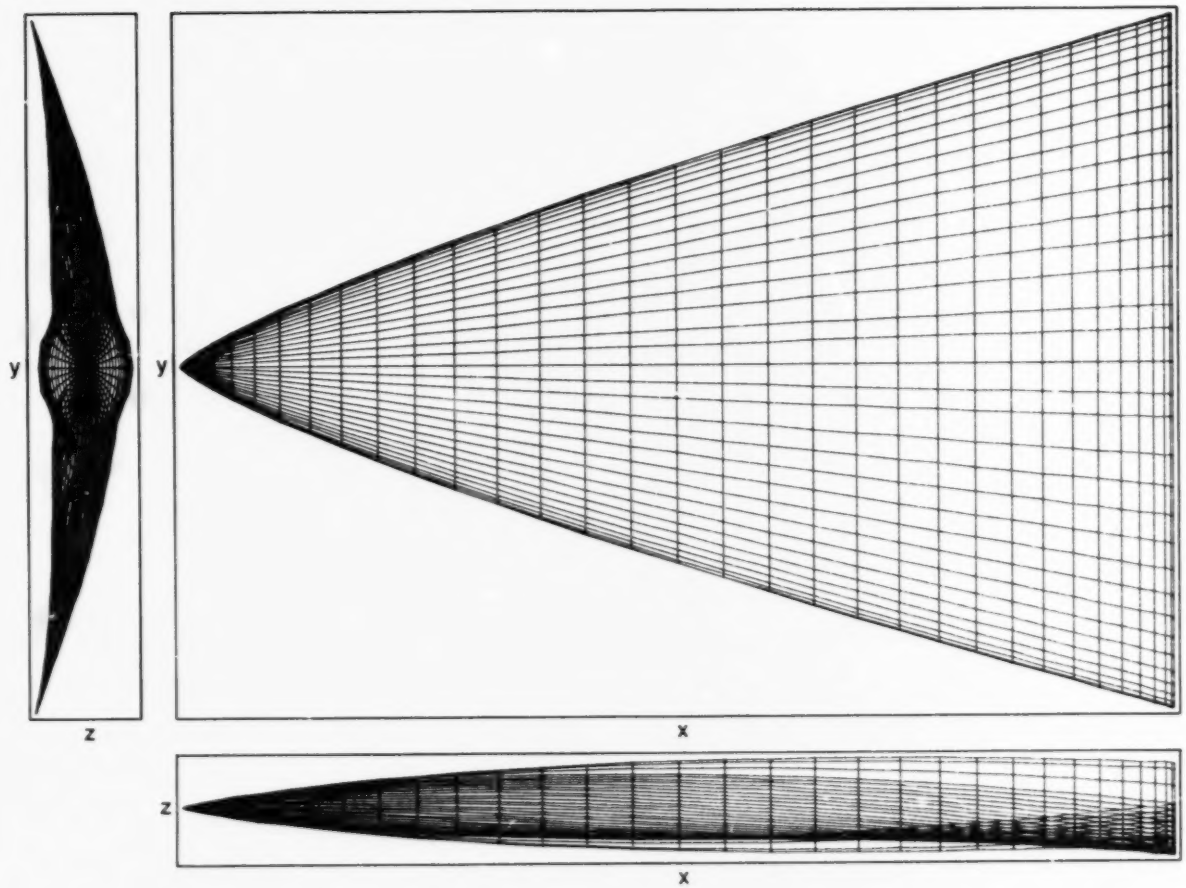

Figure 14 Three-view representation of blended wing-body geometry: Body 3.

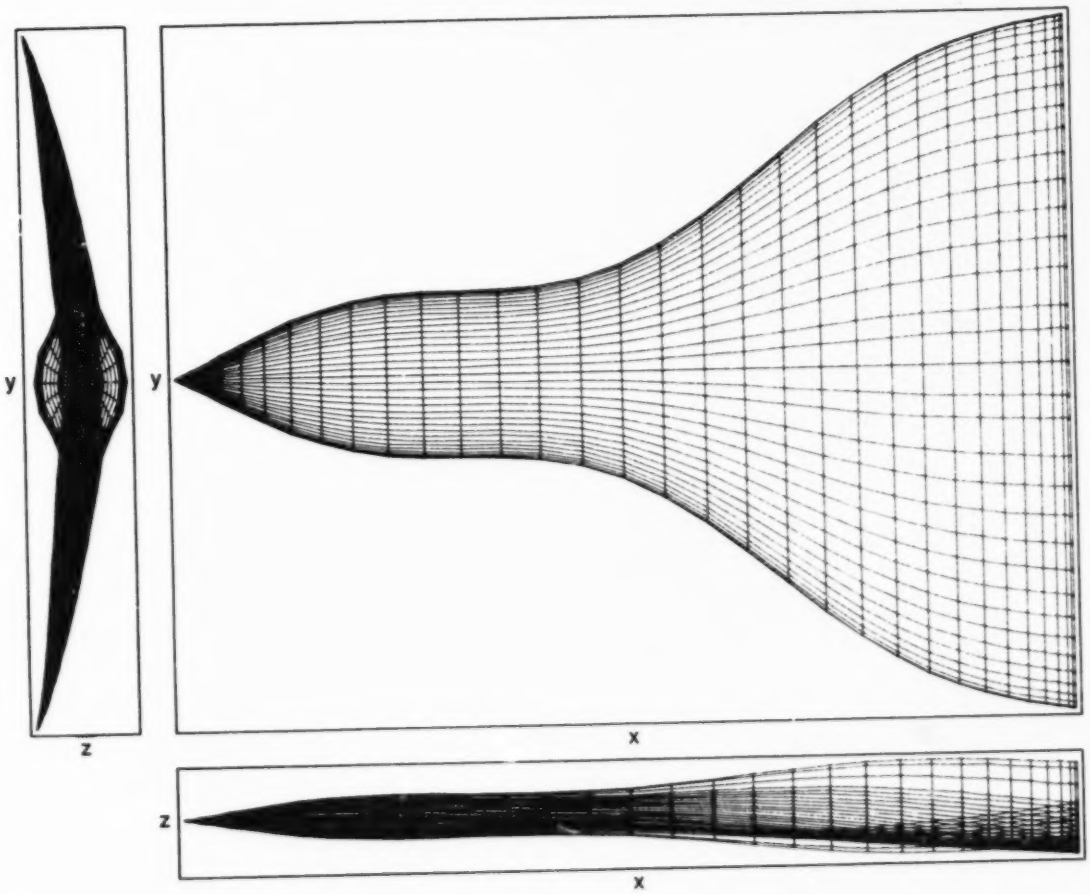

Figure 15 Three-view representation of blended wing-body geometry with complex planforms: Body 4.

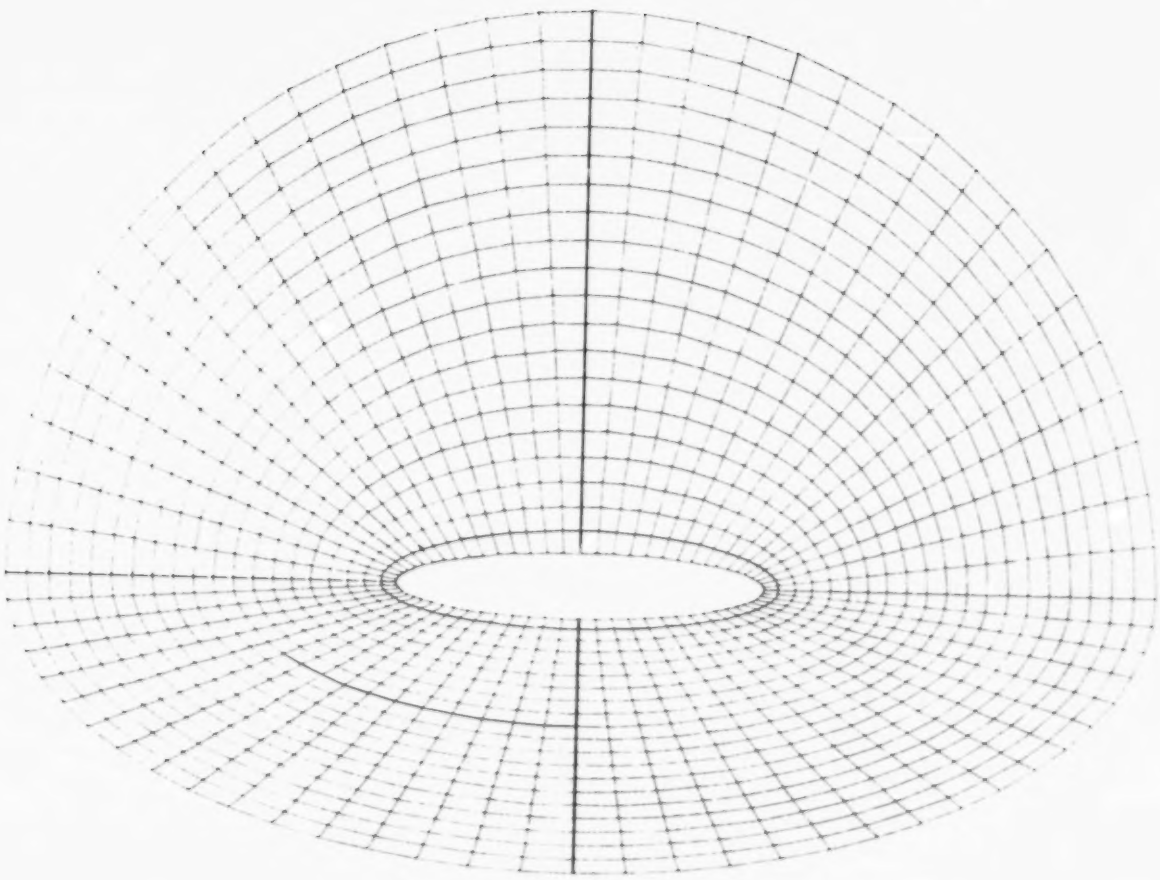

Figure 16 Sectional grid for elliptic body.

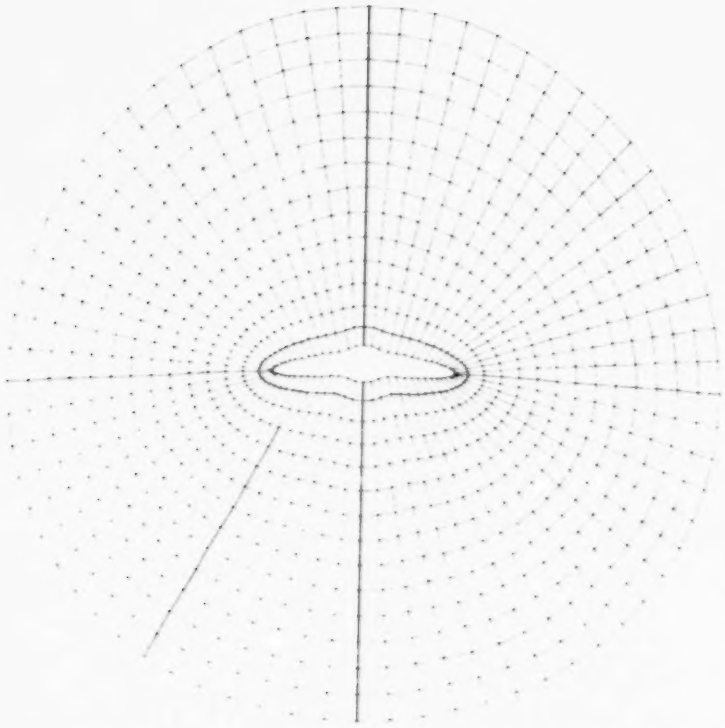

Figure 17.a Station at midlength of body.

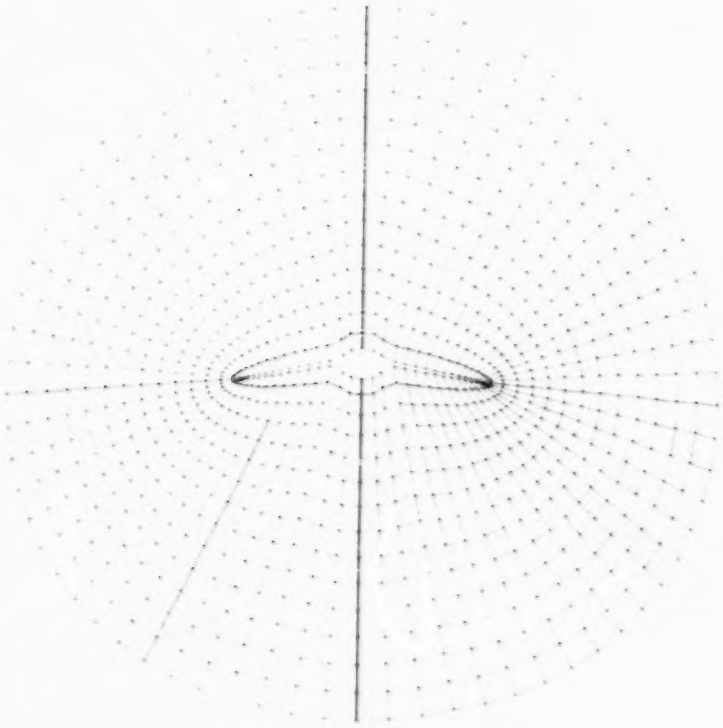

Figure 17.b Station near base.

Figure 17 Sectional grids for Body 3.

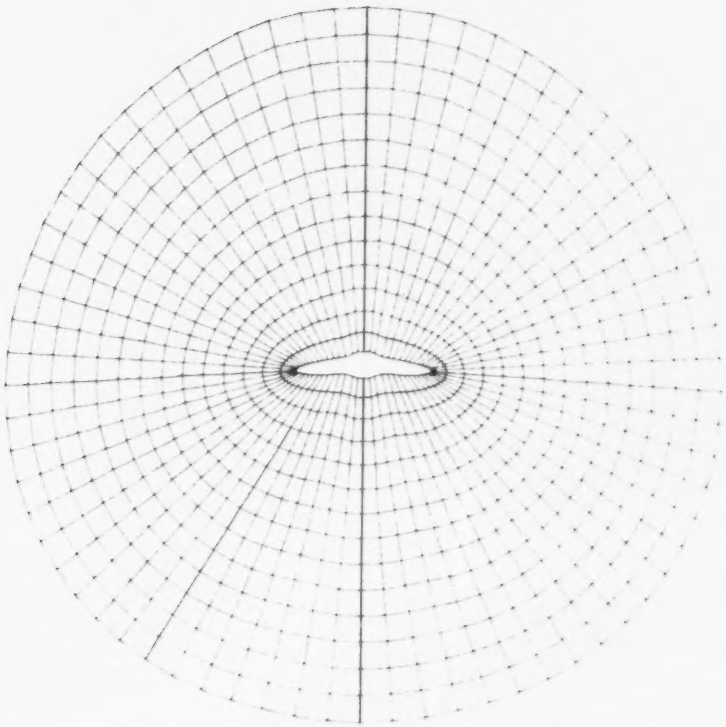

Figure 18.a Station at midlength of body.

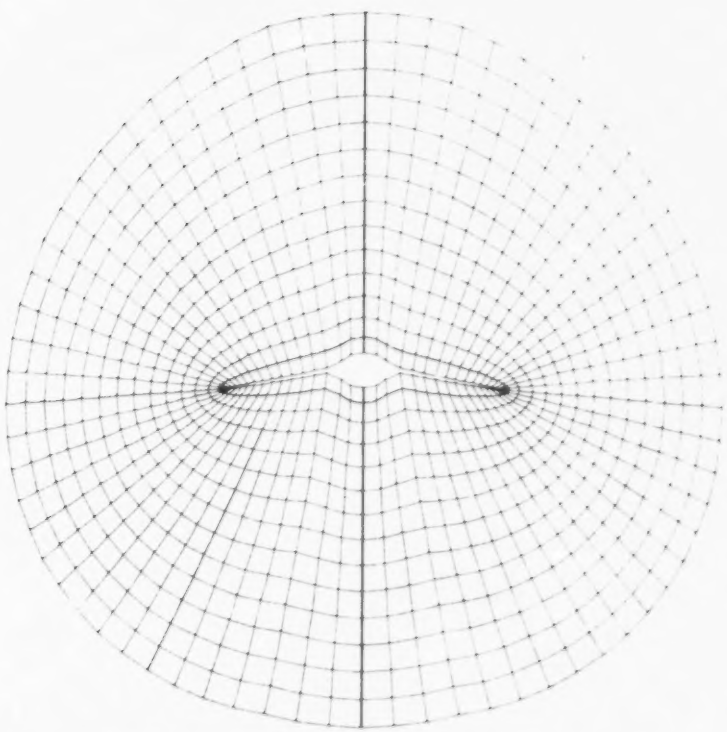

Figure 18.b Station near base.

Figure 18 Sectional grids for Body 4.

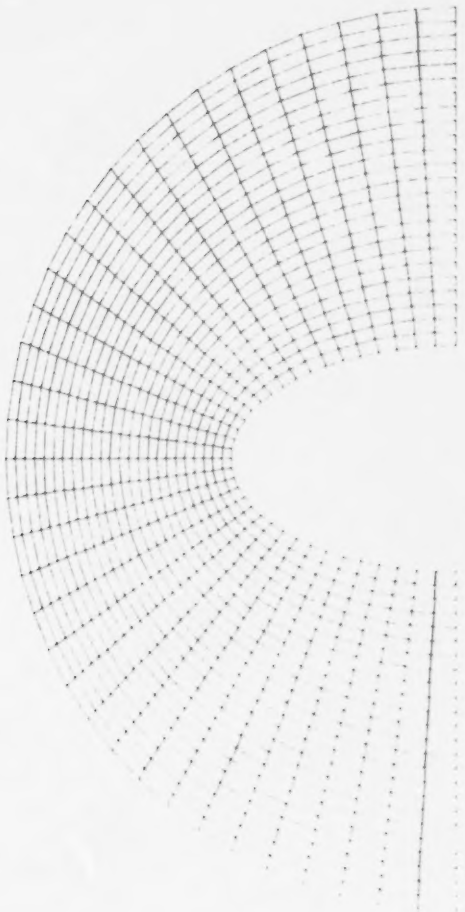

Figure 19 Sectional grid for semi-elliptic cylinder.

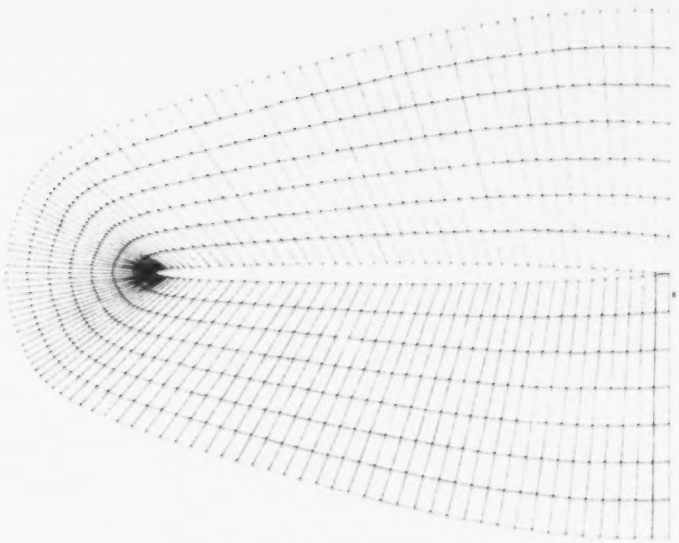

Figure 20 Grid in chord-wise plane of supersonic wing.

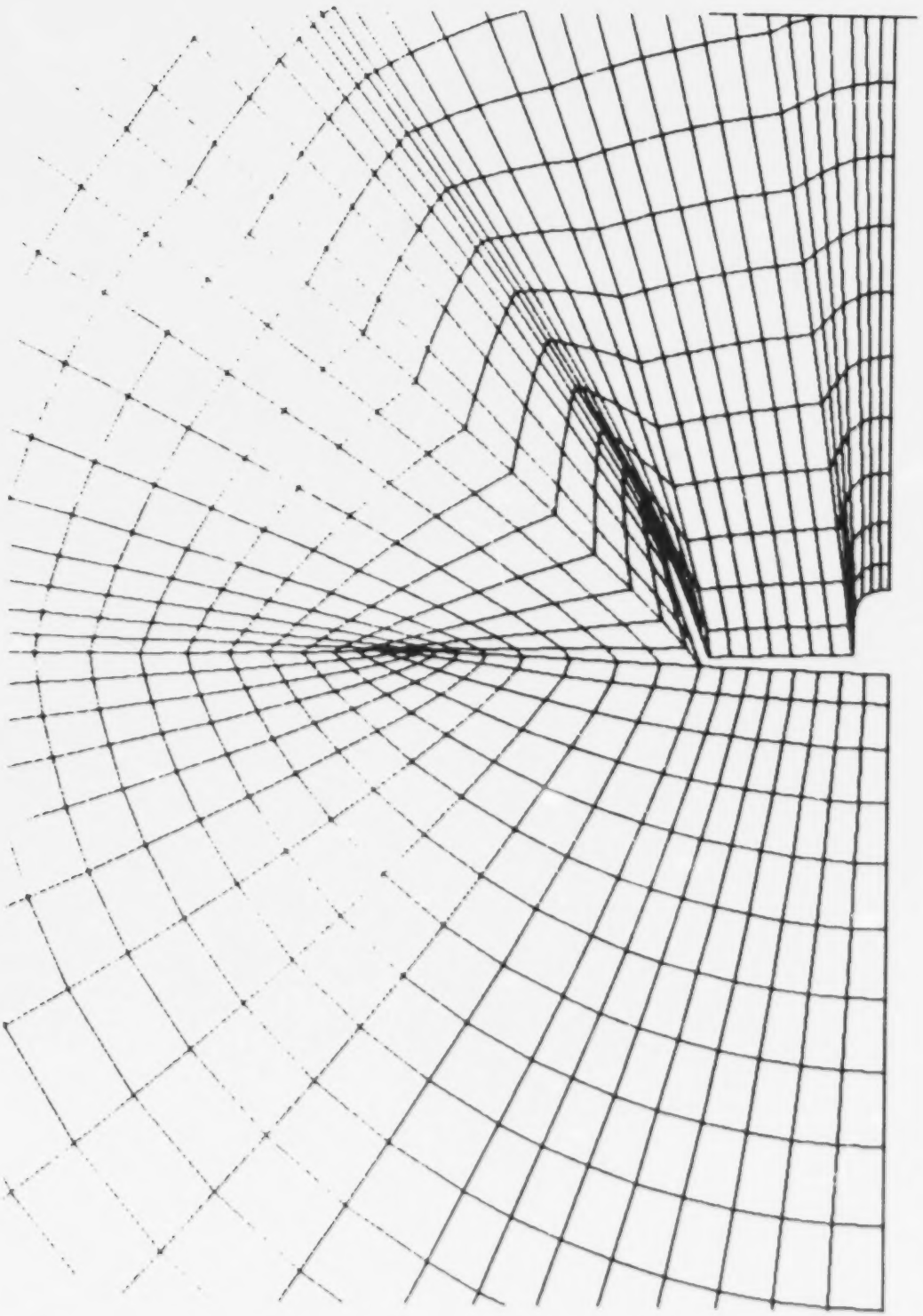

Figure 21.a Grid in section containing vertical stabilizer.

Figure 21 Grids for fighter aircraft configuration.

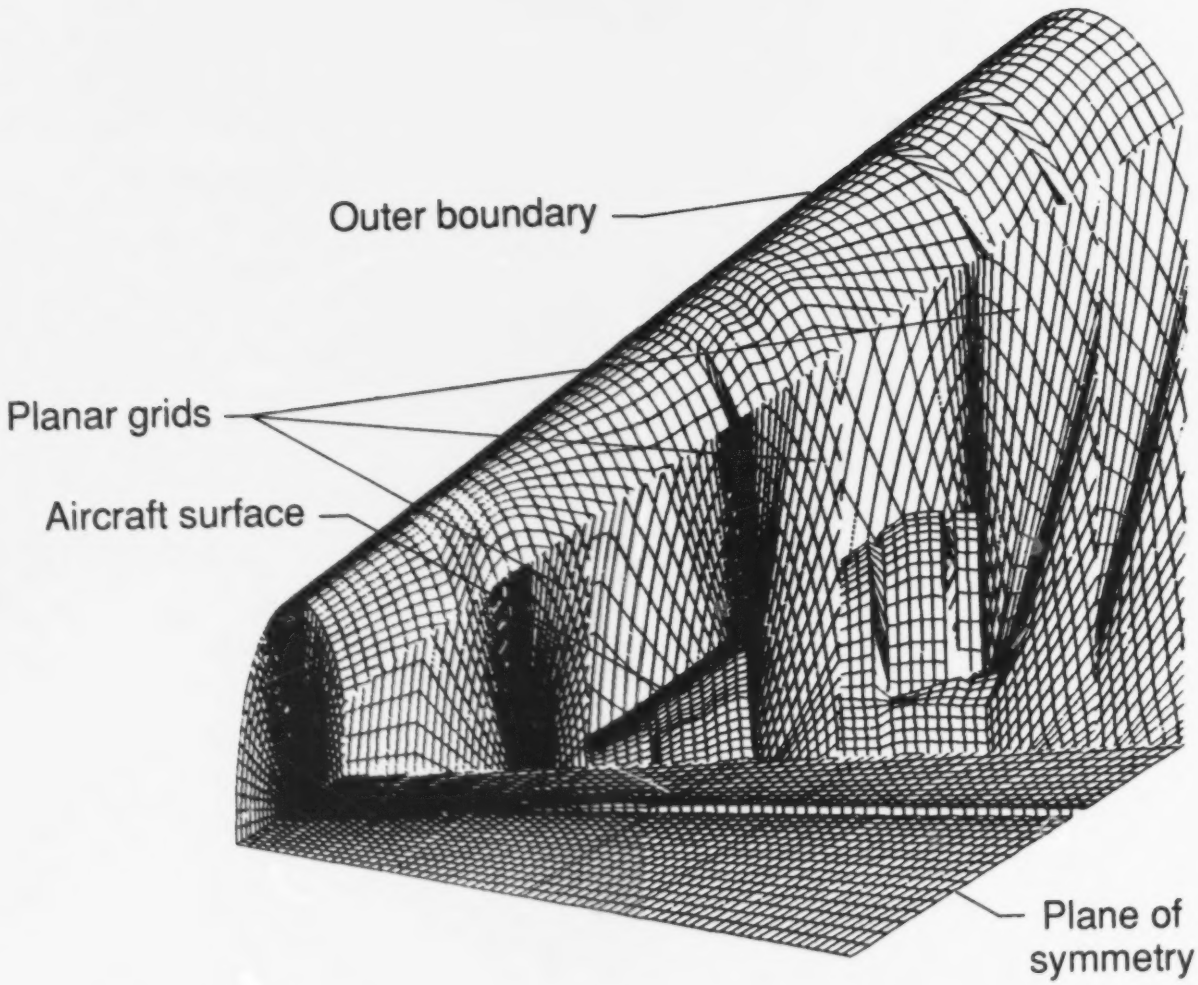

Figure 21.b Cut-away view of three-dimensional grid.

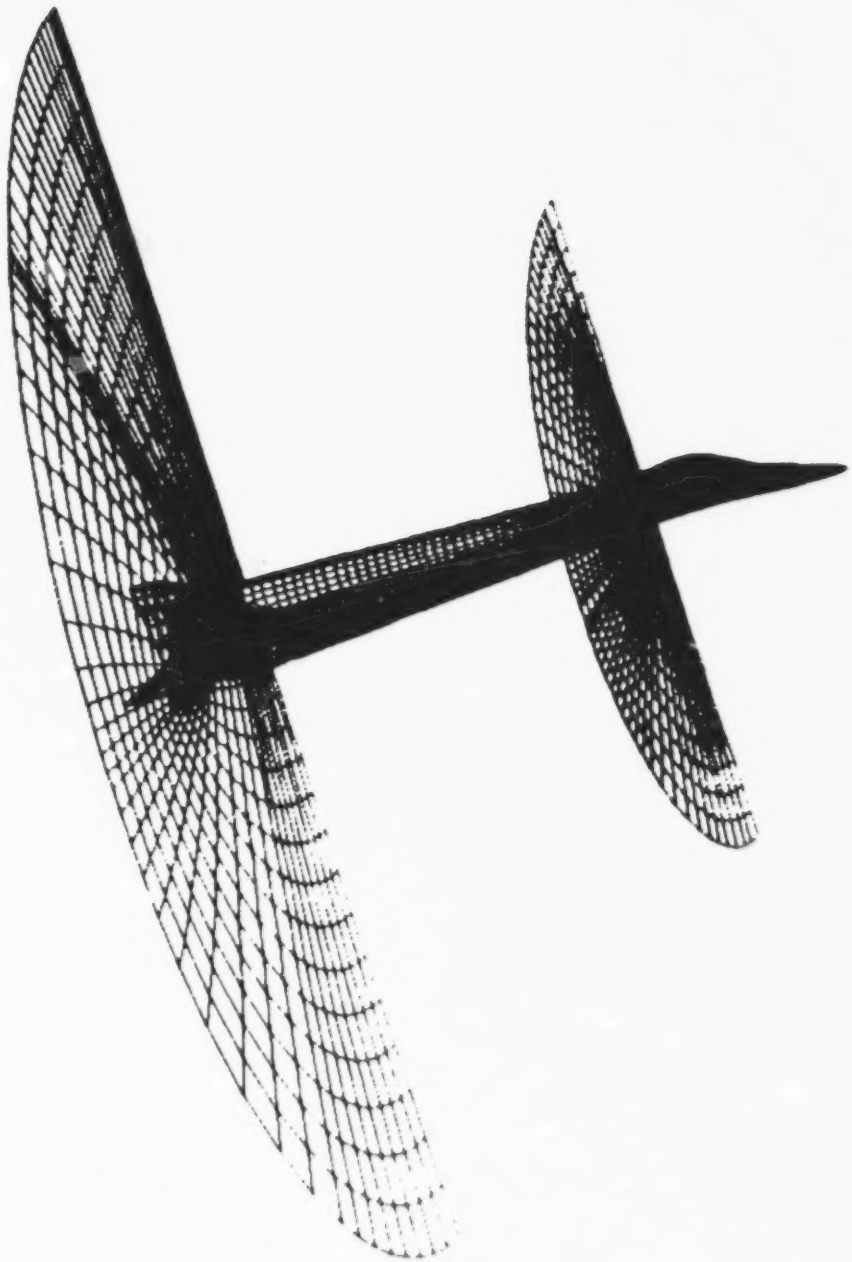

Figure 21.c Fighter aircraft with two planar grids.

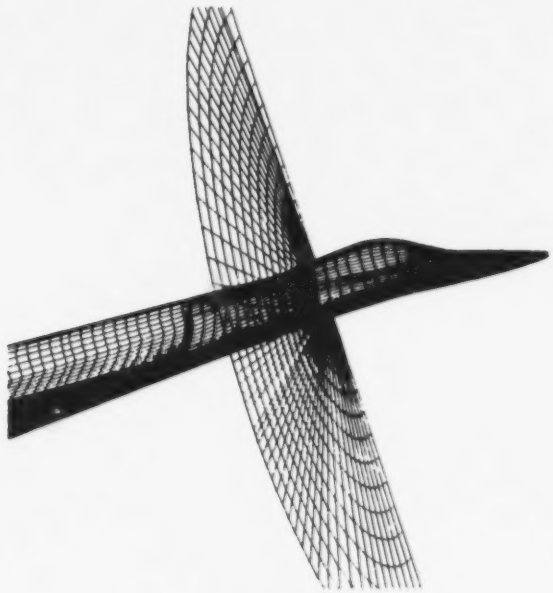

Figure 21.d Planar grid at canopy.

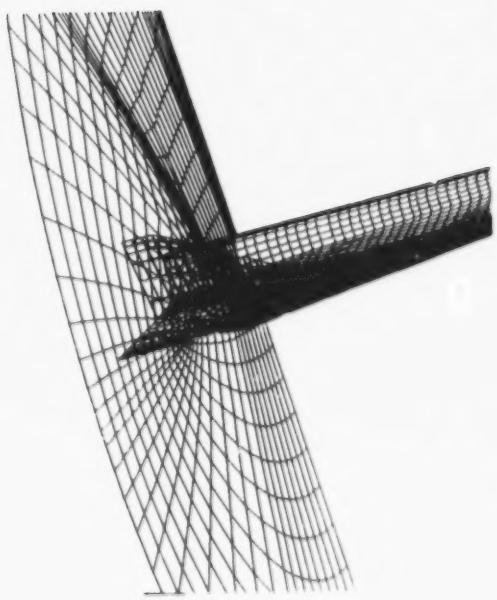

Figure 21.e Planar grid at tail.

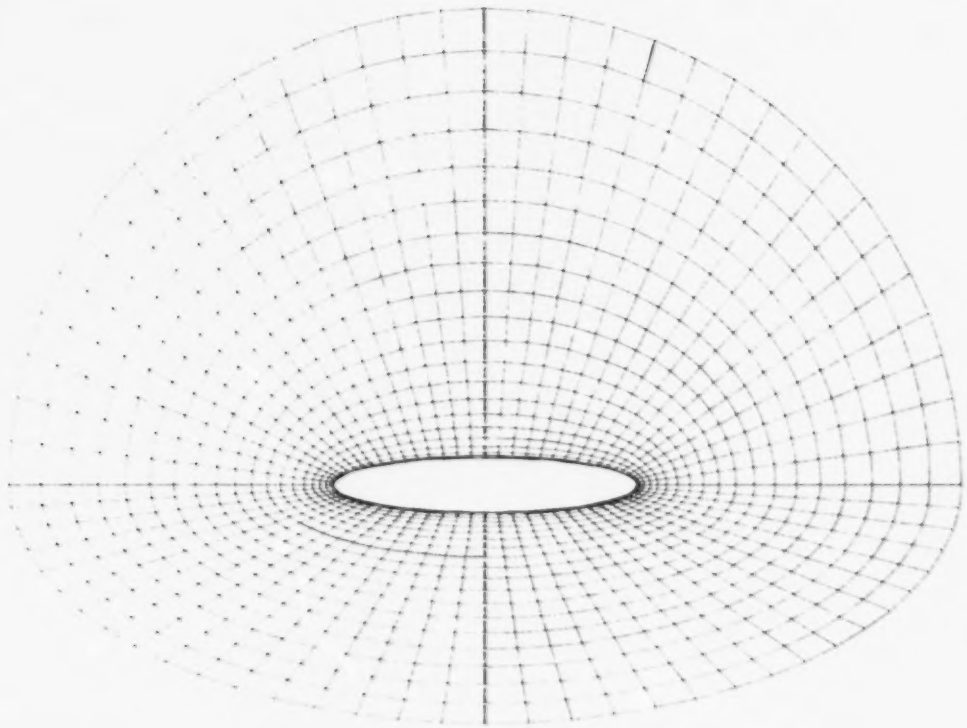

Figure 22.a Grid line concentration using m = 1.8.

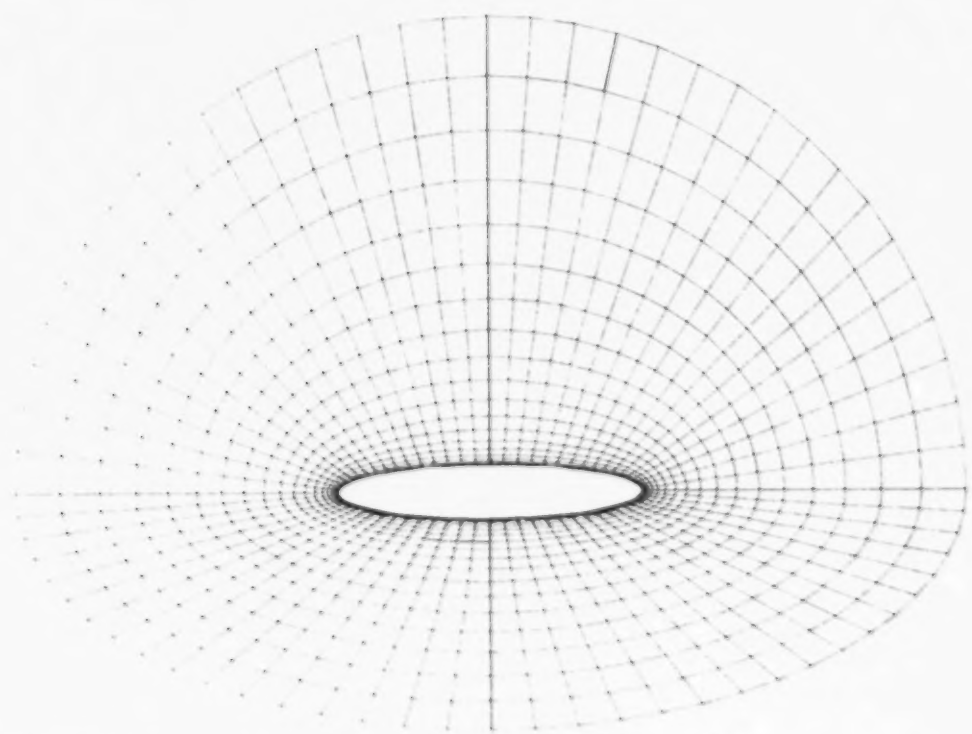

Figure 22.b Grid line concentration using m = 2.2.

Figure 22 Grid line concentration near surface of elliptic body.

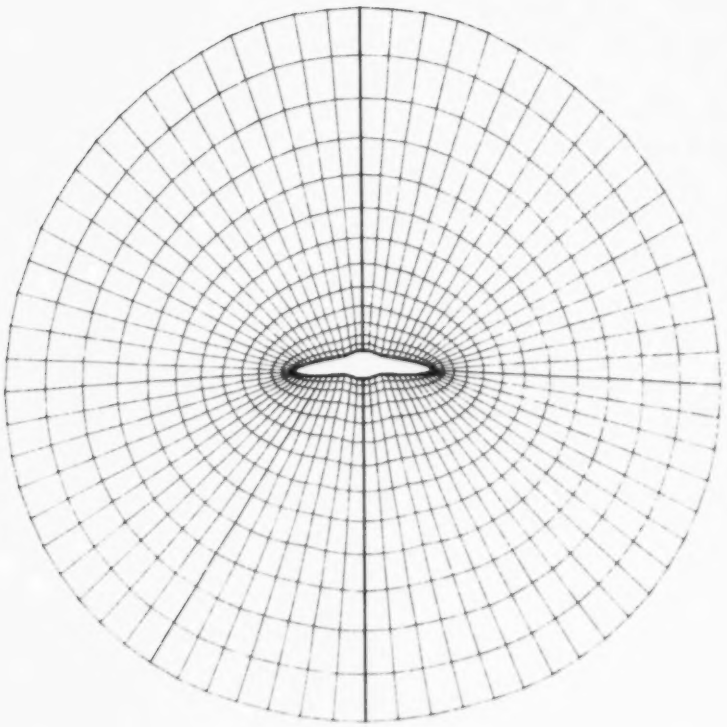

Figure 23.a Grid line concentration at midlength, m = 2.0.

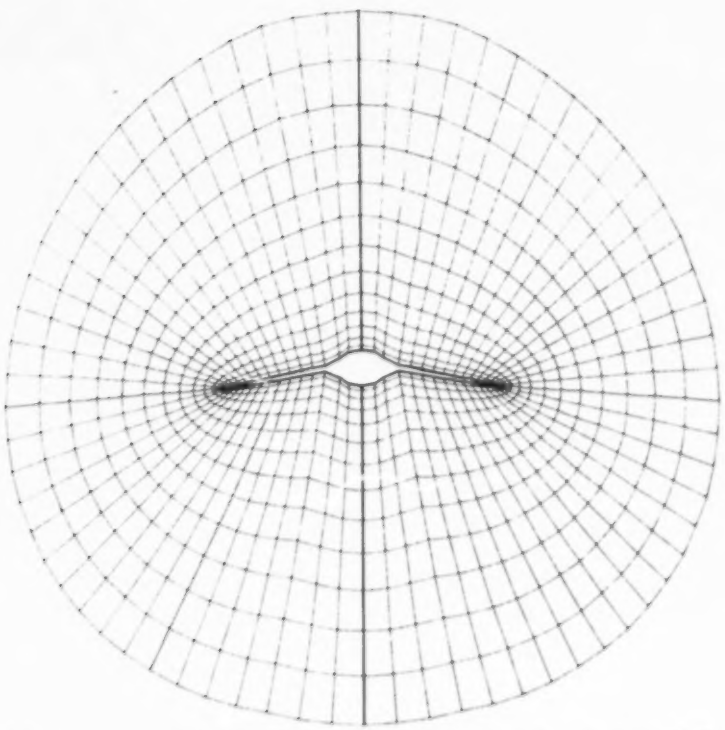

Figure 23.b Grid line concentration near base, m = 2.0.

Figure 23 Grid line concentration near surface of blended wing-body geometry.

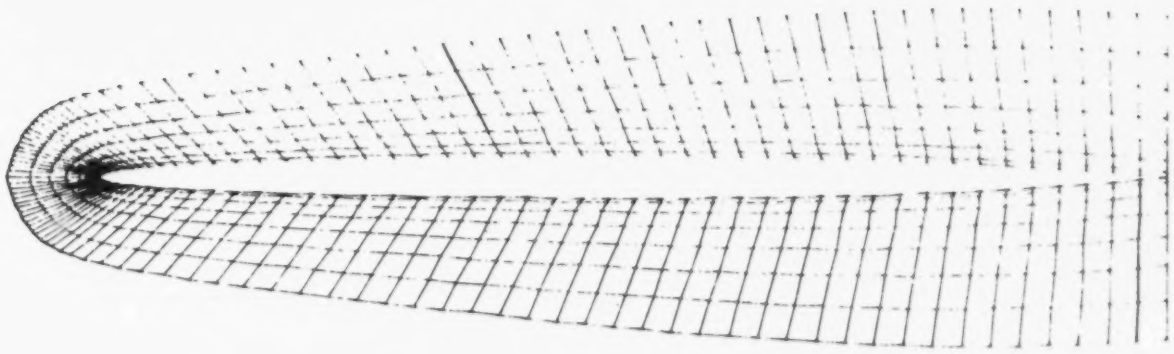

Figure 24 Grid line concentration for supersonic wing, m = 1.8.

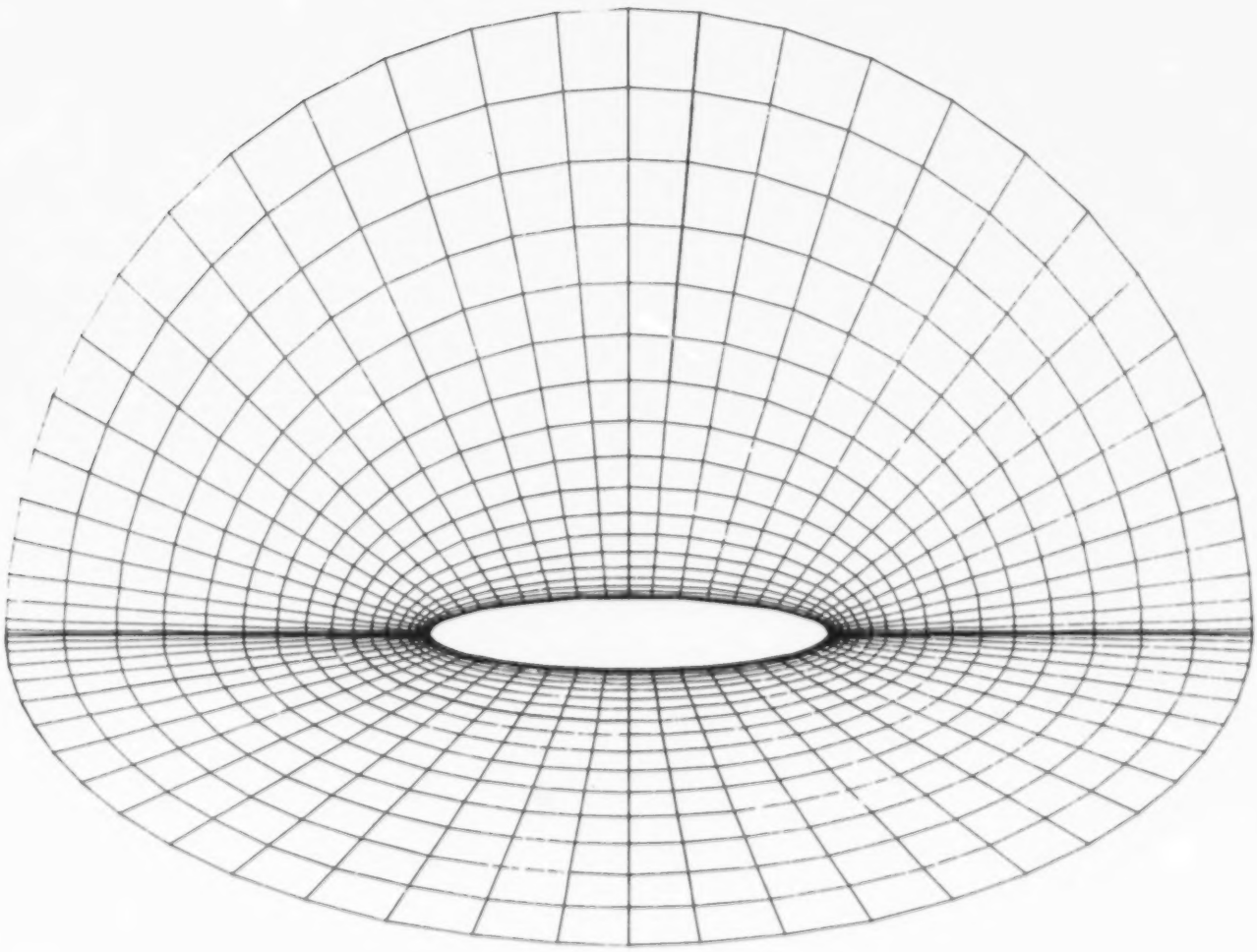

Figure 25 Grid lines clustered at tip of elliptic body.

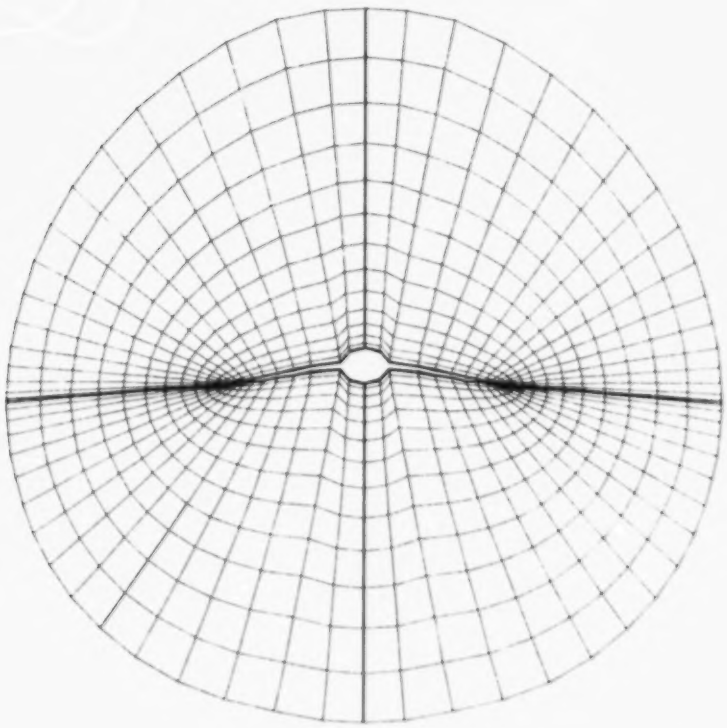

Figure 26 Grid lines clustered at wing tips of blended wing-body geometry.

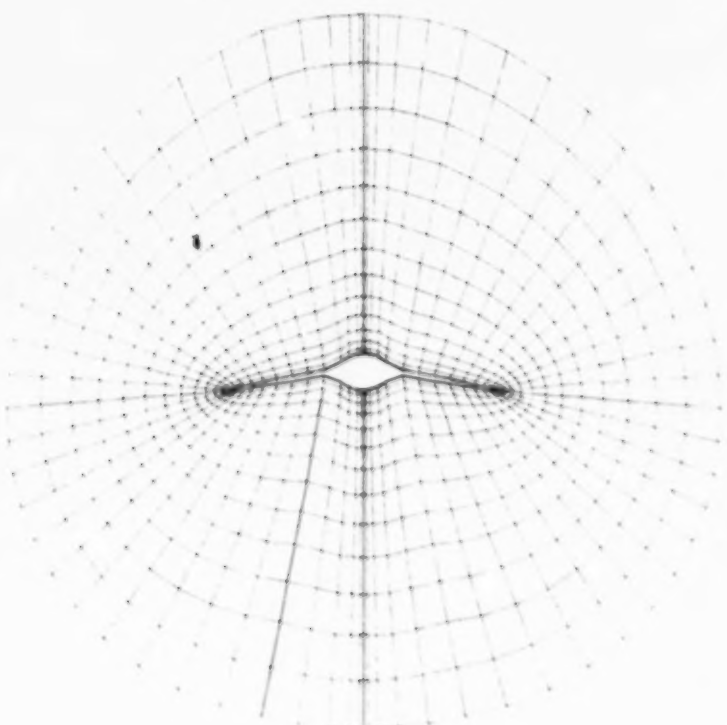

Figure 27 Grid line clustering at plane of symmetry of blended wing-body geometry.

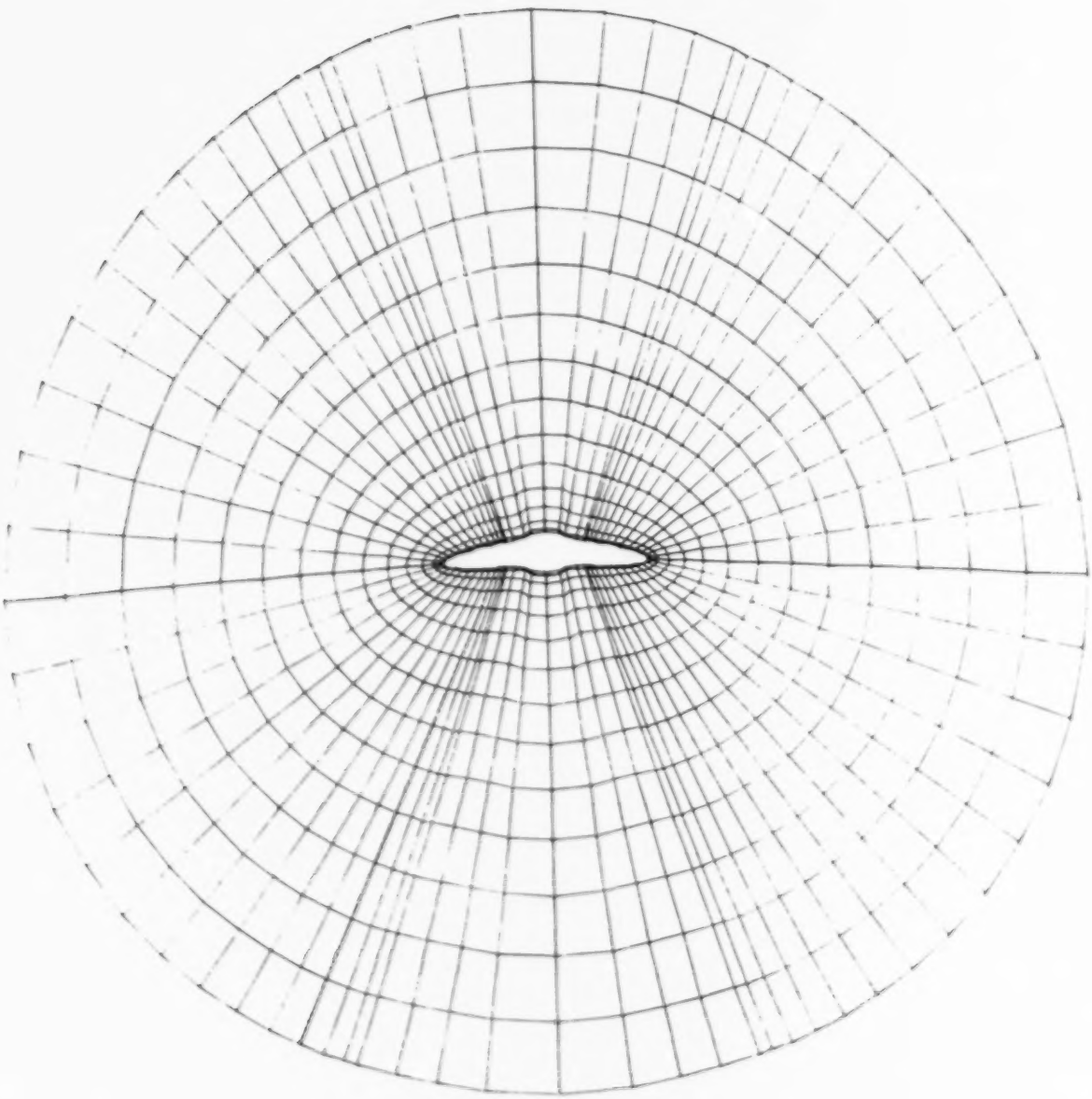

Figure 28 Grid line clustering at arbitrary location on blended wing-body geometry.

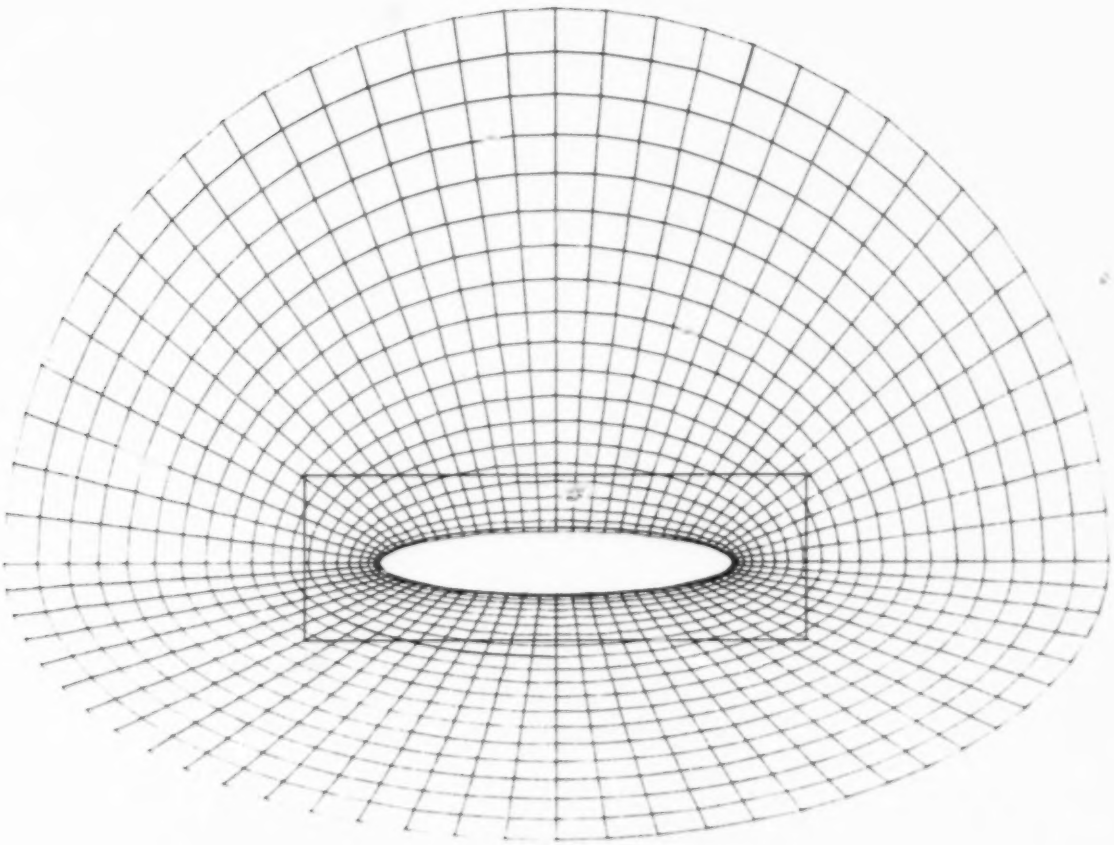

Figure 29 Partially orthogonalized grid for elliptic body.

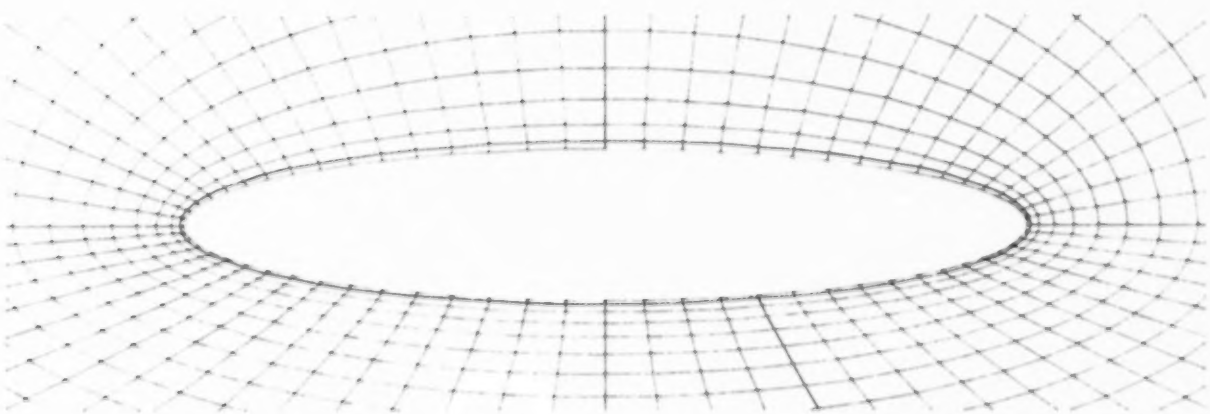

Figure 30 Orthogonality near surface of elliptic body.

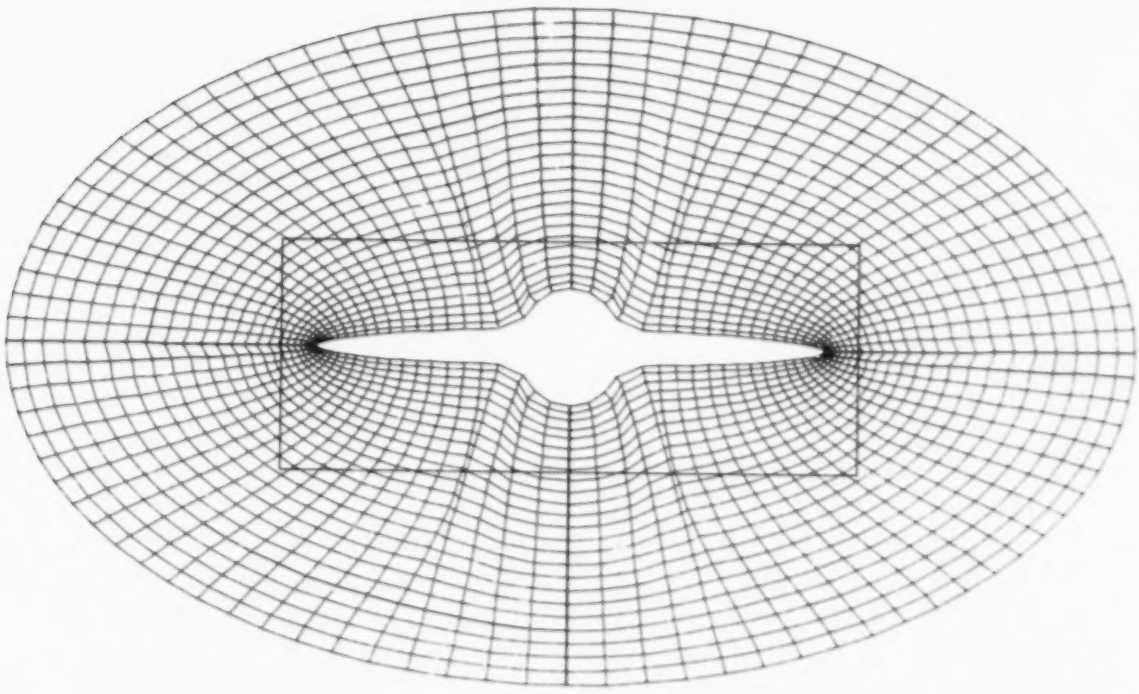

Figure 31 Orthogonal grid for blended wing-body geometry.

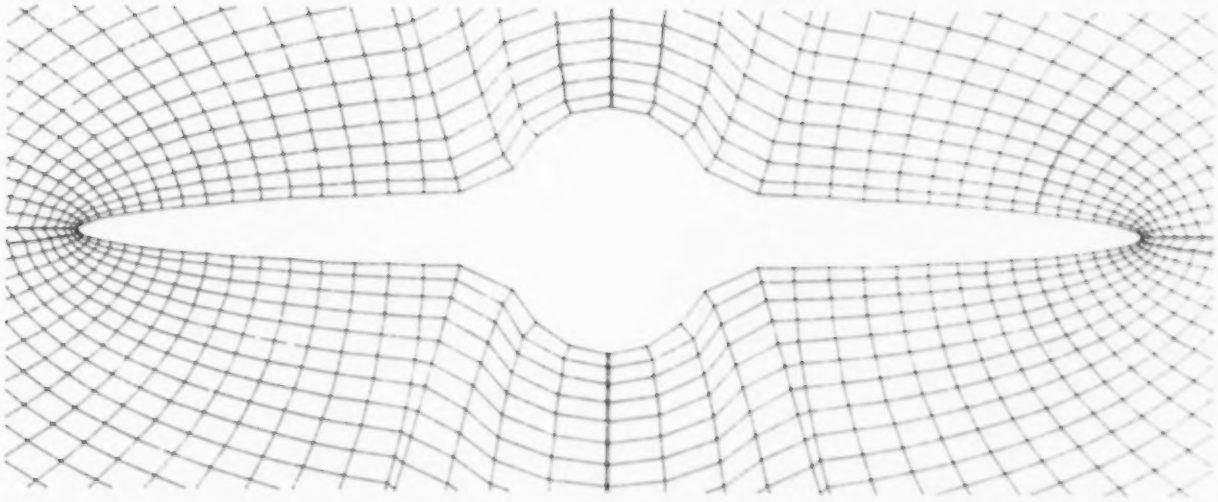

Figure 32 Orthogonality near surface of blended wing-body geometry.

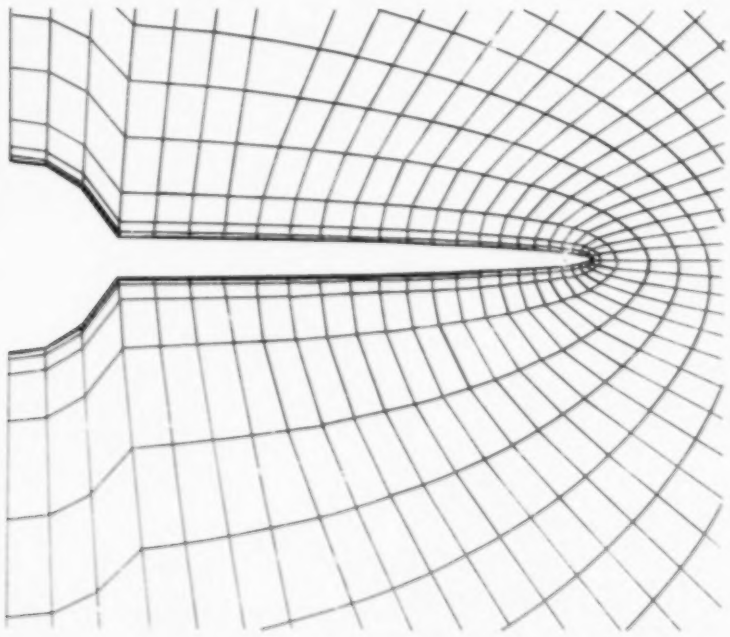

Figure 33 Orthogonalized grid for discretely input wing-body configuration.

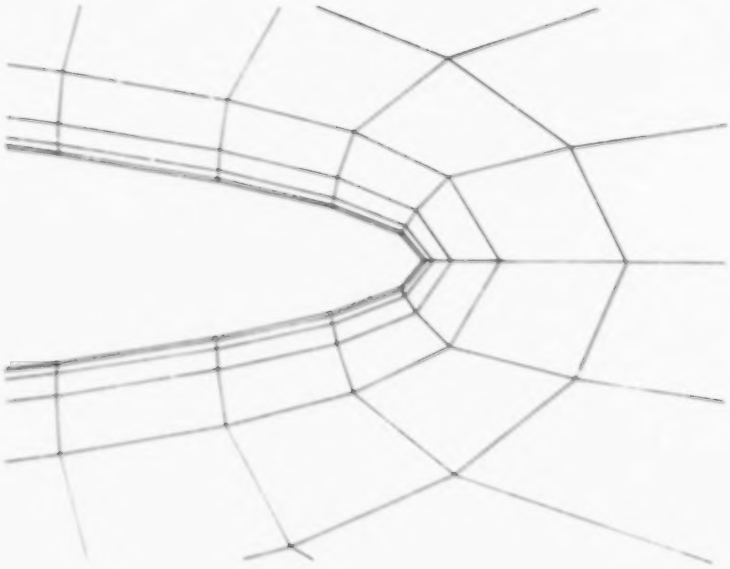

Figure 34 Orthogonal grid at wing-tip of discrete wing-body configuration.

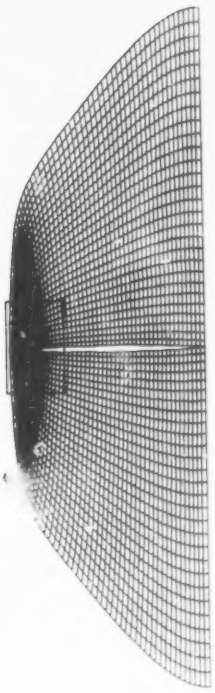

Figure 35 Orthogonal C-type grid for supersonic wing.

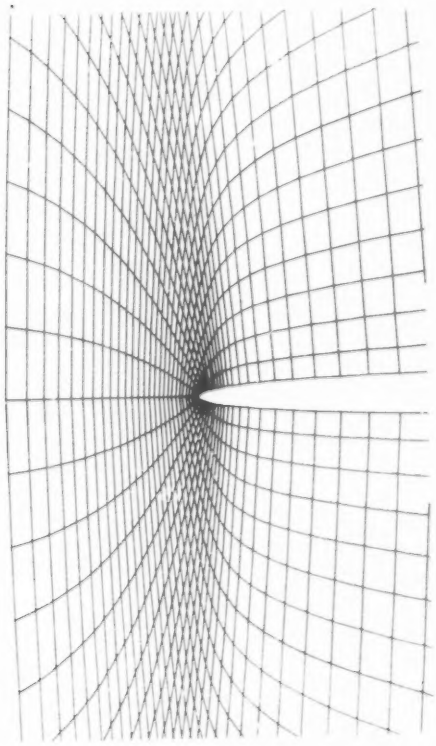

Figure 36 Orthogonality near leading edge of supersonic wing.

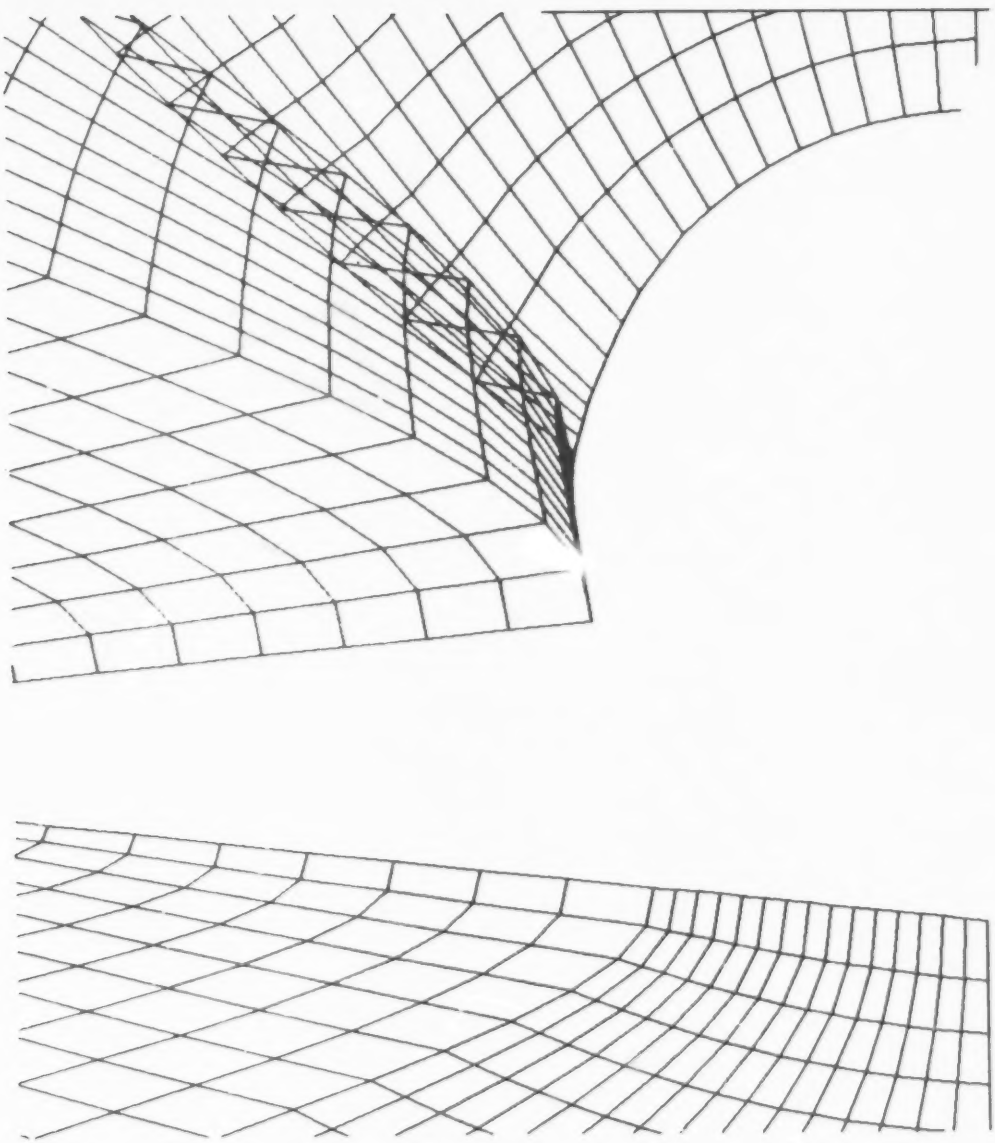

Figure 37 Intersection of orthogonal trajectories in corner regions.

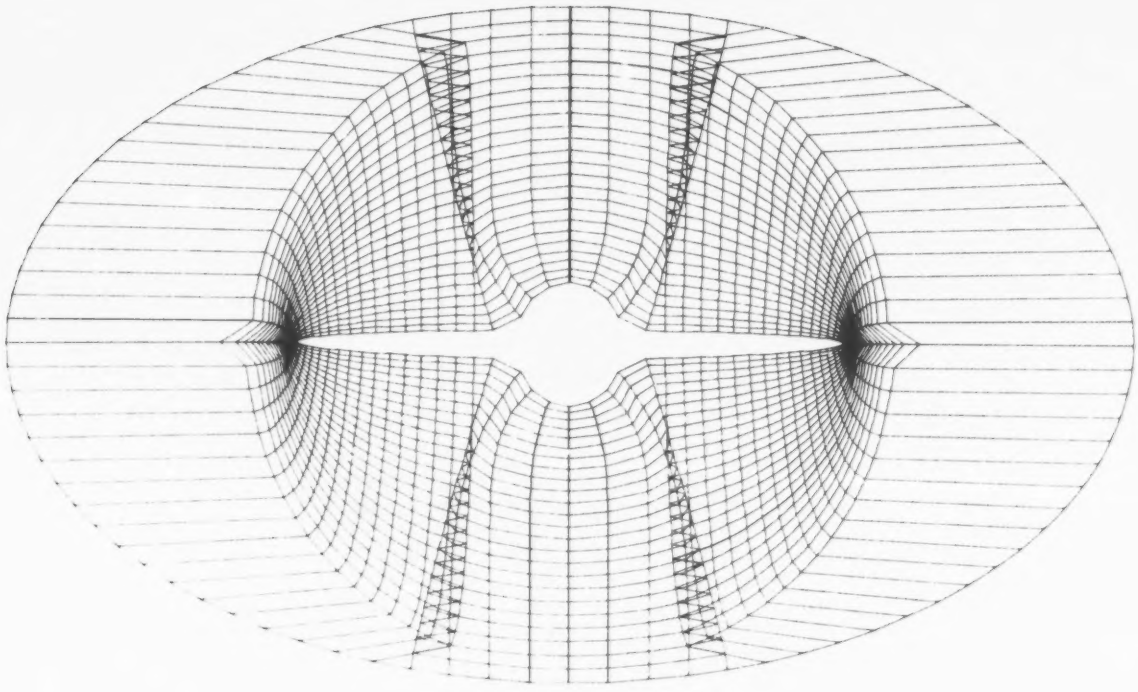

Figure 38 Intersection of trajectories in concave regions and grid distortion.

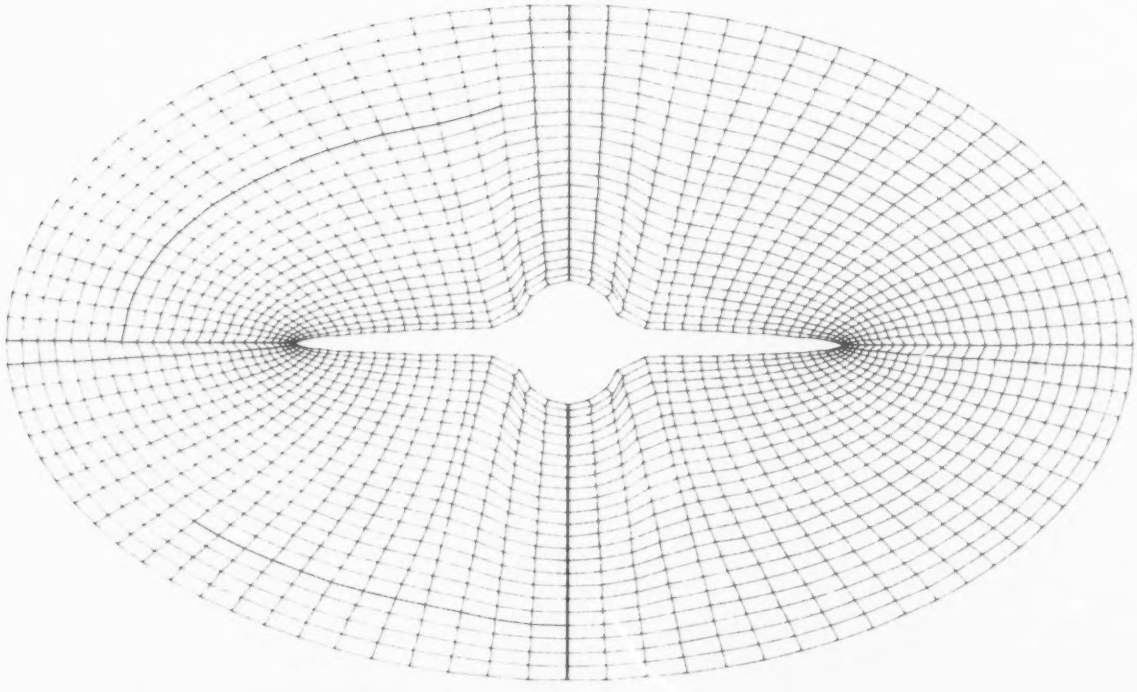

Figure 39 Smooth grid with intersections removed.

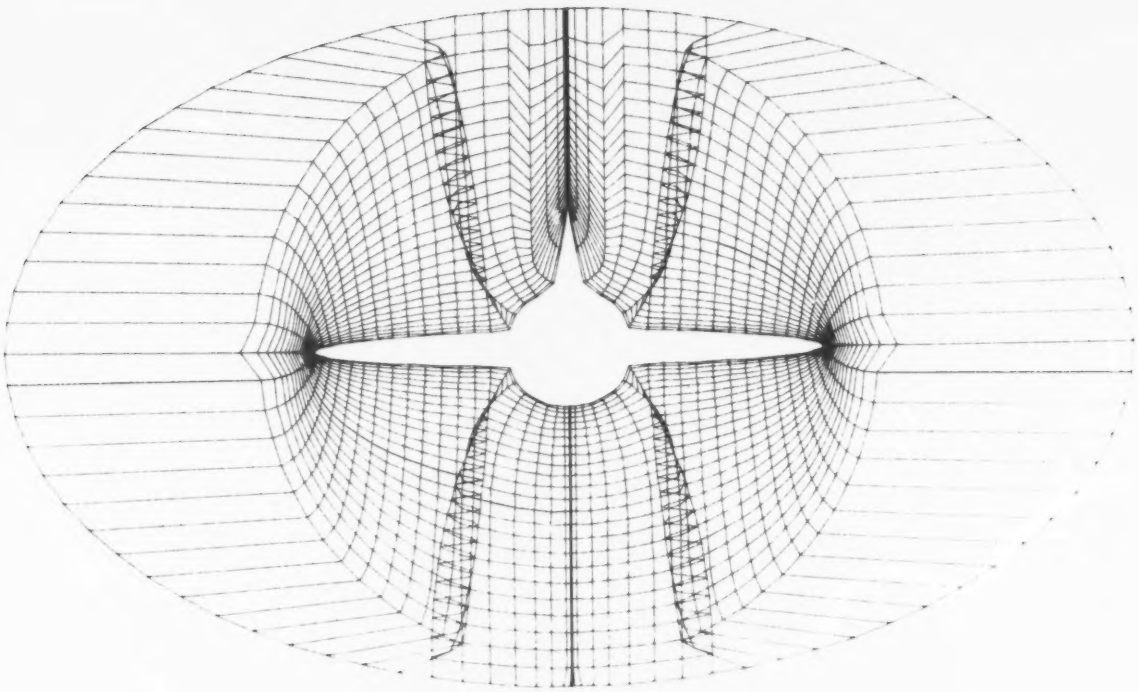

Figure 40 Intersecting normal trajectories for section containing vertical stablizer.

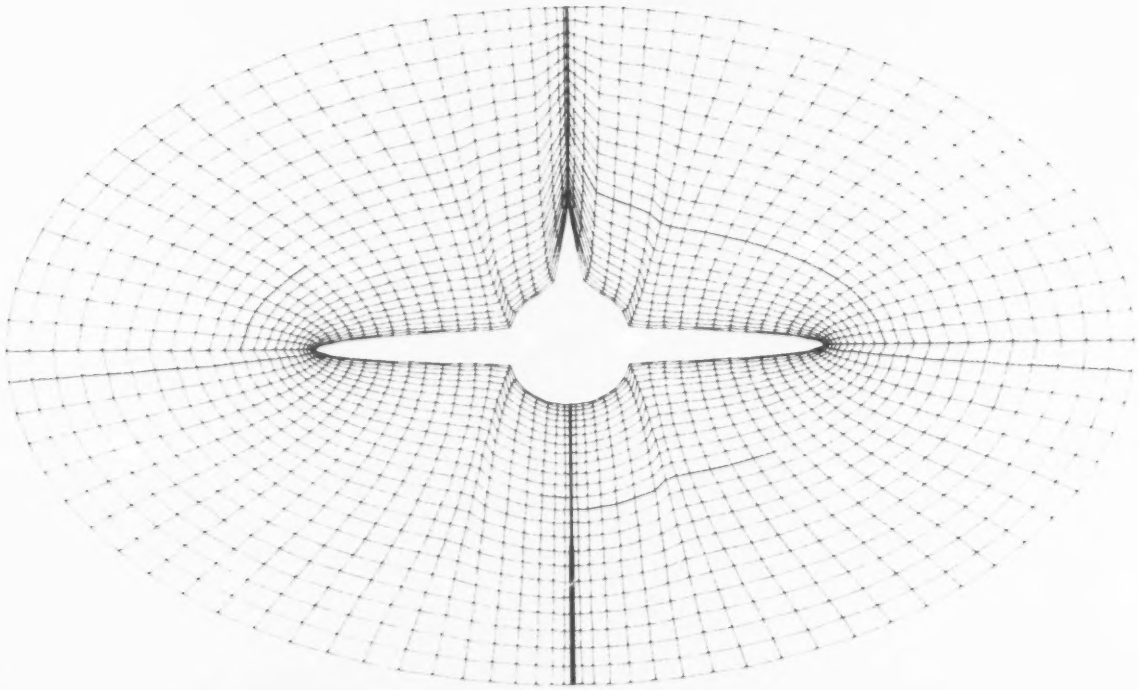

Figure 41 Smooth grid for section with vertical stabilizer with intersections and distortions removed.

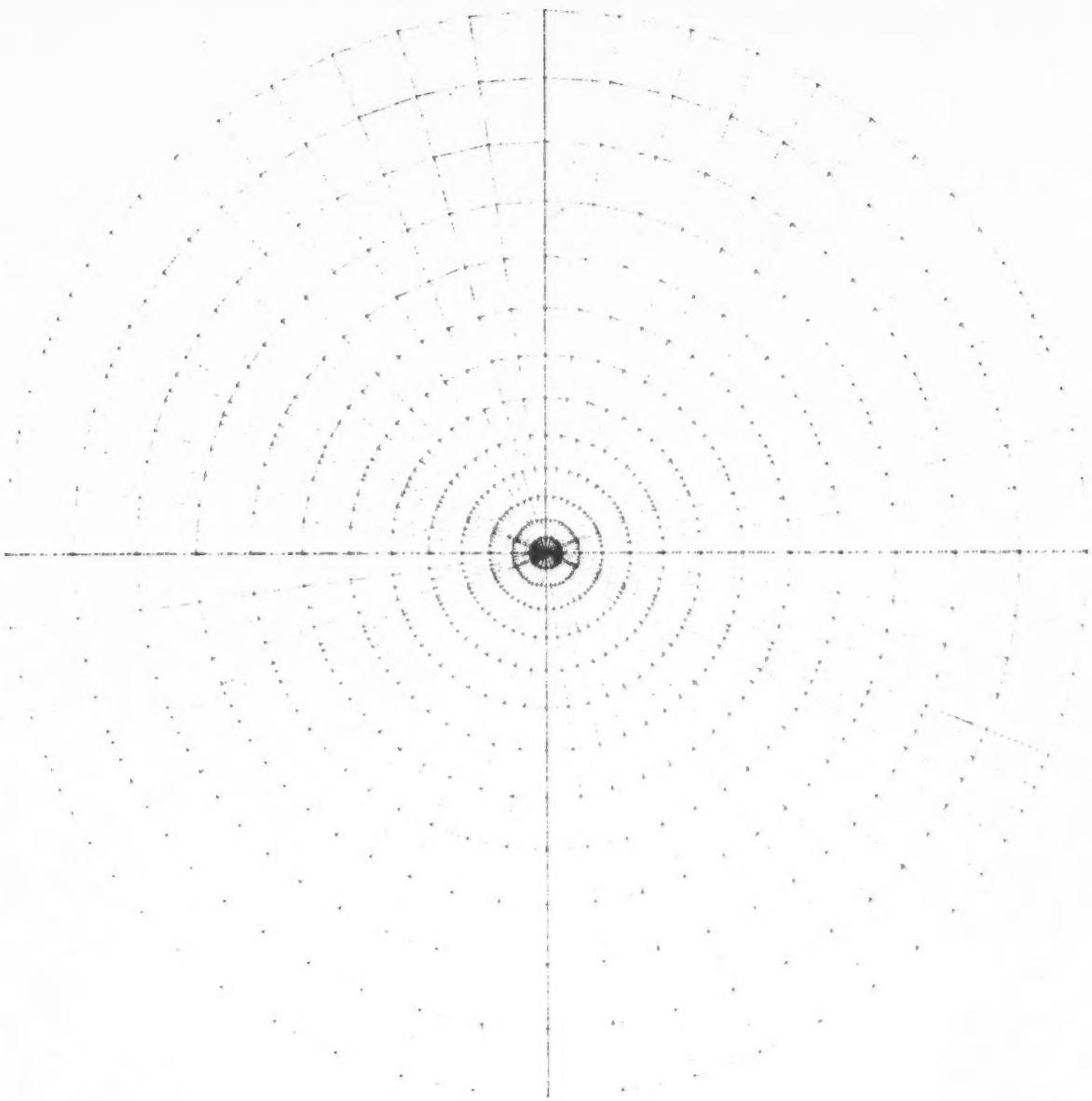

Figure 42 Polar-like grid for nozzle with grid clustering.

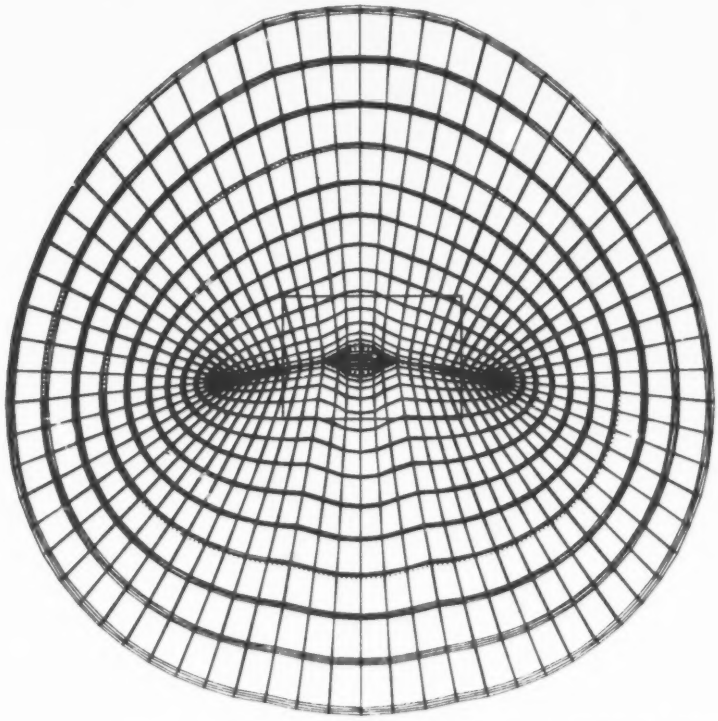

Figure 43 Grids in exhaust area behind base of blended wing-body configuration.

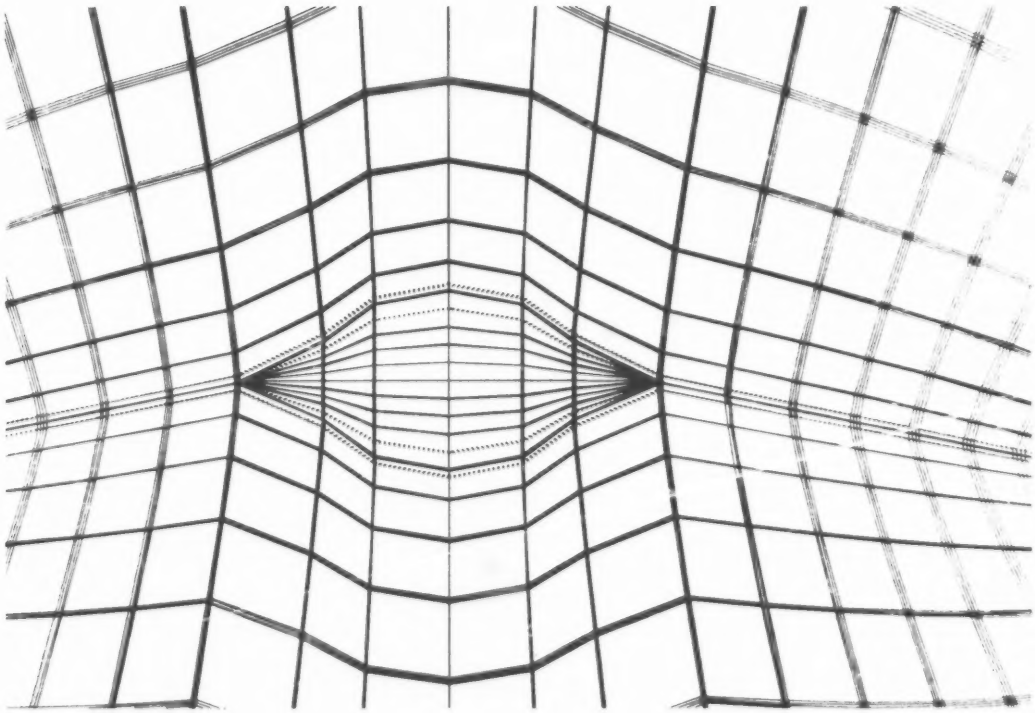

Figure 44 Continuity between inner and outer grids in exhaust area.

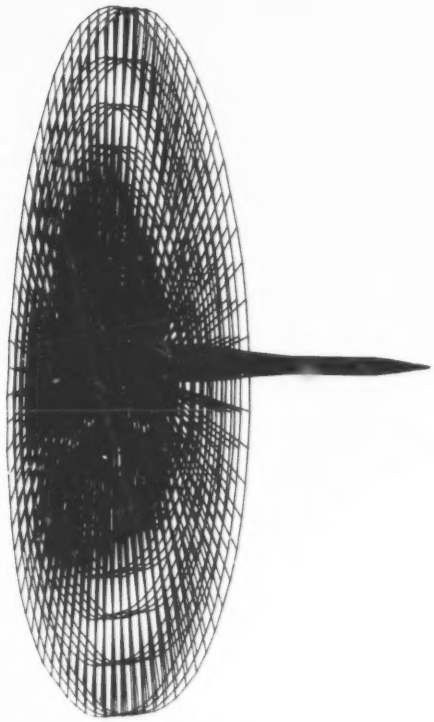

Figure 45 Stacked grids in exhaust region.

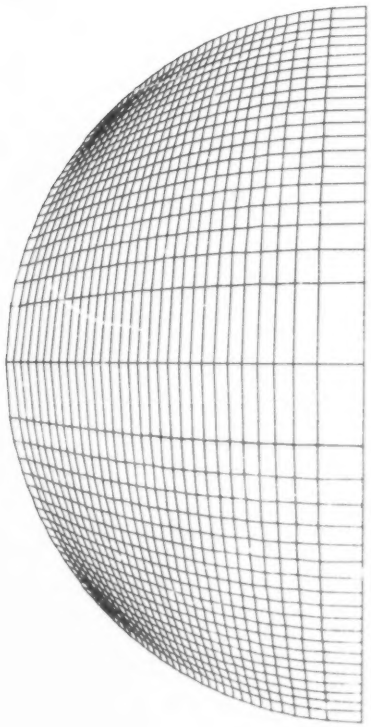

Figure 46 Sectional grid for duct with circular cross-section.

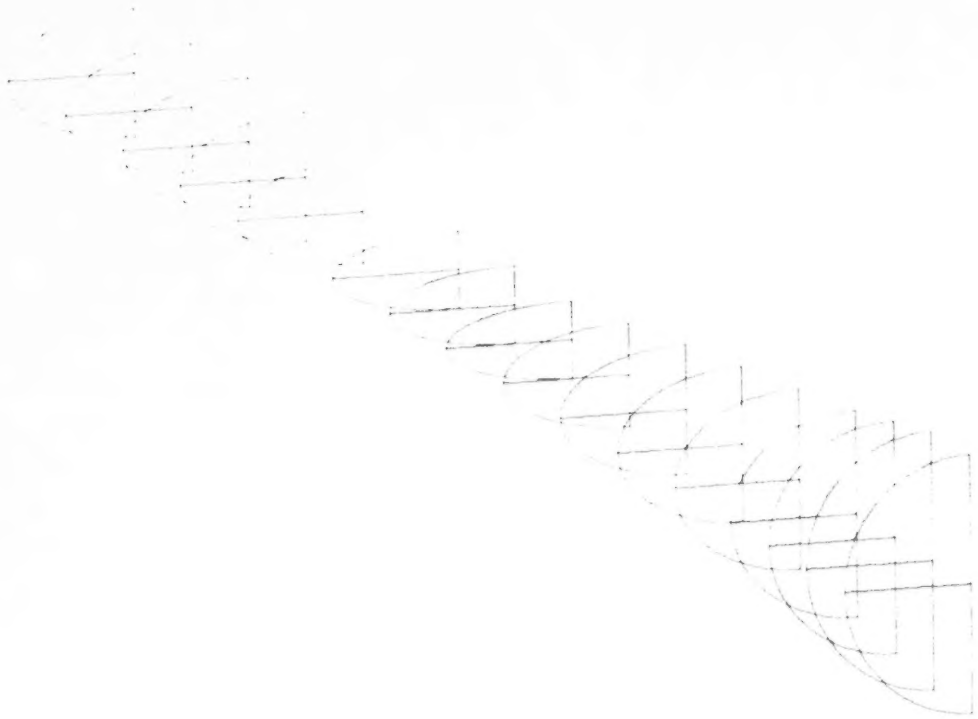

Figure 47 Duct geometry with varying cross-sectional shapes.

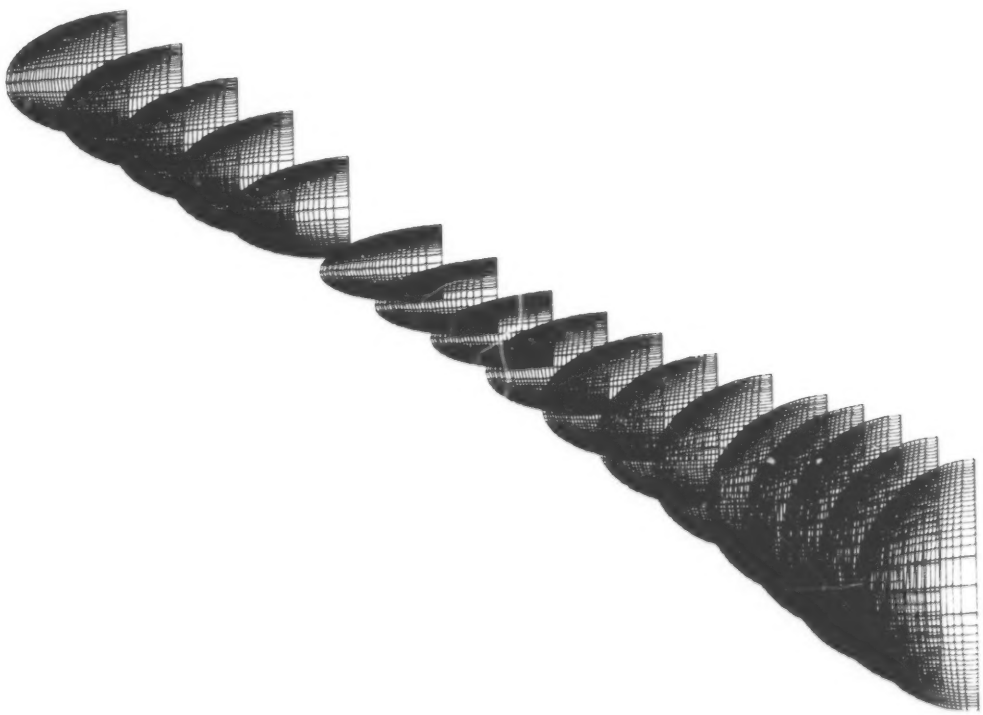

Figure 48 Duct configuration with sectional grids.

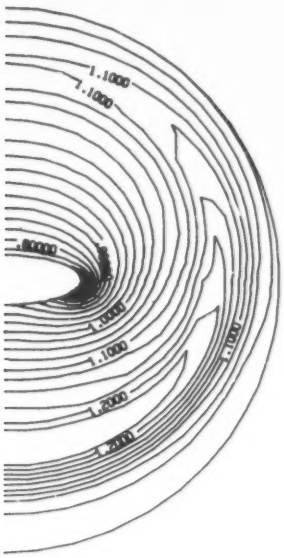

Figure 49 Computed pressure contours for elliptic body M = 1.6, $\alpha = 6^{o}$.

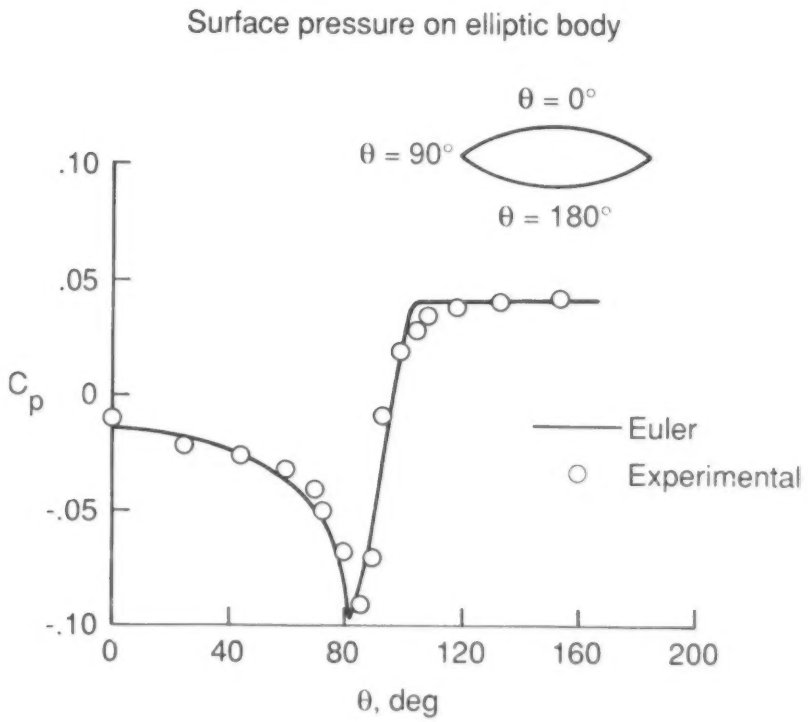

Figure 50 Computed surface pressure on elliptic body. $0^{o} \leq \theta \leq 180^{o}$, M = 2.5, $\alpha = 5^{o}$.

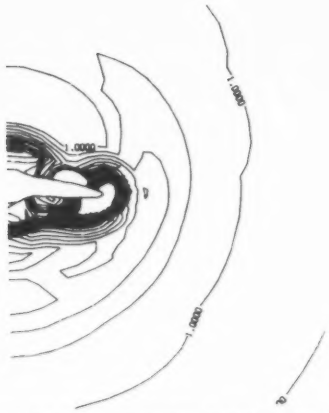

Figure 51 Computed pressure contours for blended wing-body. M = 3.0, $\alpha = 3^{o}$.

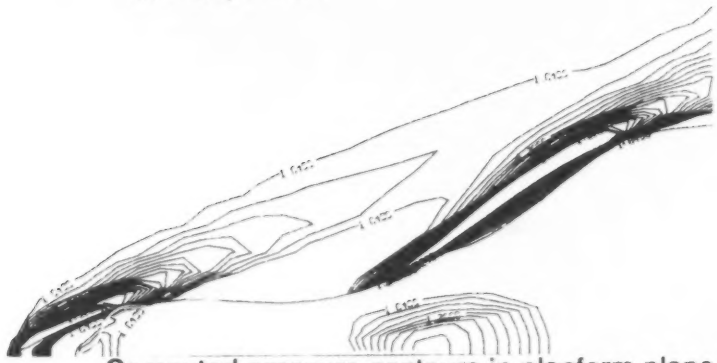

Figure 52 Computed pressure contours in planform plane of blended wing-body configuration. M = 3.0, $\alpha = 3^{o}$.

Figure 53 Computed pressure contours for fighter aircraft. M = 1.8, $\alpha = 5^{o}$.

NASA
National Aeronautics and Space Administration

Report Documentation Page

1. Report No.	2. Government Accession No.	3. Recipient's Catalog No.
NASA CR-4242		

4. Title and Subtitle
An Algebraic Homotopy Method for Generating Quasi-Three-Dimensional Grids for High-Speed Configurations

5. Report Date
July 1989

6. Performing Organization Code

7. Author(s)
Anutosh Moitra

8. Performing Organization Report No.

10. Work Unit No.
505-80-11-05

9. Performing Organization Name and Address
High Technology Corporation
28 Research Drive
Hampton, VA 23666

11. Contract or Grant No.
NAS1-18240

13. Type of Report and Period Covered
Contractor Report

12. Sponsoring Agency Name and Address
National Aeronautics and Space Administration
Langley Research Center
Hampton, VA 23665-5225

14. Sponsoring Agency Code

15. Supplementary Notes
Langley Technical Monitor: Julius E. Harris

16. Abstract

A fast and versatile procedure for algebraically generating boundary conforming computational grids for use with finite-volume Euler flow solvers is presented. A semi-analytic homotopic procedure is used to generate the grids. Grids generated in two-dimensional planes are stacked to produce quasi-three-dimensional grid systems. The body surface and outer boundary are described in terms of surface parameters. An interpolation scheme is used to blend between the body surface and the outer boundary in order to determine the field points. The method. albeit developed for analytically generated body geometries is equally applicable to other classes of geometries. The method can be used for both internal and external flow configurations, the only constraint being that the body geometries be specified in two-dimensional cross-sections stationed along the longitudinal axis of the configuration. Techniques for controlling various grid parameters, e.g., clustering and orthogonality are described. Techniques for treating problems arising in algebraic grid generation for geometries with sharp corners are addressed. A set of representative grid systems generated by this method is included. Results of flow computations using these grids are presented for validation of the effectiveness of the method.

17. Key Words (Suggested by Author(s))	18. Distribution Statement
Algebraic grids Homotopy Euler	Unclassified - Unlimited Subject Category 34

19. Security Classif. (of this report)	20. Security Classif. (of this page)	21. No. of pages	22. Price
Unclassified	Unclassified	84	A05

NASA-Langley, 1989

For sale by the National Technical Information Service, Springfield, Virginia 22161-2171